Summer 8-2-2012

High Frequency Study of Magnetic Nanostructures

Abhishek Srivastava
University of New Orleans, abhi.alld@gmail.com

Recommended Citation

Srivastava, Abhishek, "High Frequency Study of Magnetic Nanostructures" (2012). *University of New Orleans Theses and Dissertations*. 1530.
https://scholarworks.uno.edu/td/1530

High Frequency Study of Magnetic Nanostructures

A Thesis

Submitted to the Graduate Faculty of the
University of New Orleans
in partial fulfillment of the
requirements for the degree of

Master of Science
In
Applied Physics

by

Abhishek Srivastava

M.Sc Banaras Hindu University, India, 2005
M.Tech Indian Institute of Technology Delhi, India, 2008

August, 2012

Acknowledgements

I am extremely grateful to Prof. Leonard Spinu for being a great advisor and a friend. I will always be thankful to him for his advices and support which were not only related to my research but also with my personal difficulties. I enjoyed the independence and flexibility given to me by Dr. Spinu.

I would like to thank Prof. Leszek Malkinski and Prof. John Wiley for their suggestions and for being committee members to evaluate my work.

I am also thankful to my colleagues: Andrei Diaconu, Denny Lenormand and Shankar Khanal for their support. Further I would like to thank Dr. Ioan Dumitru for introducing me to the microwave measurement techniques.

I am especially thankful to Dr. Jose Vargas for his help and support throughout my stay at University of New Orleans.

Finally I am thankful to National Science Foundation for the financial support and staff of Advanced Materials Research Institute (AMRI) at the University of New Orleans for their administrative help.

Table of Contents

List of Figures

Fig 4.1.2.2.2a: Room-*T*, X-band, FMR spectra of a) MiHa, b) HaMi and c) SM-MiHa samples, measured at different angular orientations against magnetic field. The sample are positioned in such way that the angle value of $\varphi = 0°$ and 90° correspond to the magnetic field along and perpendicular to the Ni Nanowires, respectively.

Fig 4.1.2.2.2b: Low-$T = 4.4$ K, X-band, FMR spectra of a) MiHa, b) HaMi and c) SM-MiHa samples, measured at different angular orientations against magnetic field.

Fig 4.1.2.2.2c: X-band angular variation of the resonance field (H_R) for MiHa, HaMi and SM-MiHa samples measured at a) Room-*T* and b) Low-$T = 4.4$ K.
Fig 4.1.2.2.2d: X-band angular variation from $\varphi = 0°$ ($H \,||$ wires) to $\varphi = 90°$ ($H \perp$ wires) of the line-width (ΔH_{pp}) for the three samples, at room-*T* and at low-$T = 4.2$ K.

Fig 5.2.2a: The typical magnetization loops for sample S2 at different orientations of the applied magnetic field, H, at room-T.

Fig 5.2.3a: The FORC diagrams as 2D contour plot in coordinate (HC;Hu) for the samples S2, S4 and S5 are shown (left). Figure in the right side shows the 200 M(H;HR) FORCs colored waves for each sample, which the color distributions are indicating their contributions to the 2D contour plot, respectively.

Fig 5.2.4a: FMR, X-band (9.87 GHz), in the conditions of out-plane and in-plane, for the three samples at room-T.

Figure 5.2.4b: FMR angular variation, X-band (9.87 GHz), in-plane for the three samples, at room-T. Spectra for each sample at different angular orientations (Left).
Schematic diagram of the sample, 0 degree is defined along the strip direction (right-top). Angular variation of the two resonance fields for each sample (right, bottom.

Figure 5.2.5: VNA broadband (1 GHz-30 GHz) measurements at room-T. (Fig. a, b and c) The transmission parameter S21, obtained for each sample at 0° and 180° orientations.(Fig. d) Typical field dependence of the FMR spectra for sample S2, in both in-plane orientations. (Fig. e) Field dependence of the field-gap between both orientations. (Fig.f)) High frequency FMR response of these samples, with the combination of both results: FMR at X-band in-plane and out-plane, and FMR broadband, and the theoretical curves (MS = 800 Oe

List of Tables

Abstract

The work in this thesis is divided in three parts. In part one we developed electrodeposition method of Nickel Nanowire in commercial AAO template in constant current (Galvanostatic) mode, further we tried to estimate the growth rate from theory, from saturation magnetization and direct measurement from SEM image.

In part two we focused on using the Vector Network Analyzer (VNA) to measure the Ferromagnetic Resonance (FMR))of various magnetic Nanowire arrays. We employed different measurement geometries using microstripline and coplanar waveguide as microwave transmission lines.

In part three our aim was to study the magnetic properties of complex ferromagnetic system, especially the effect of interactions on dynamic properties of magnetic nanostructures (nanowire arrays and exchange biased ferromagnetic-antiferromagnetic multilayers). Our effort was centered on using ferromagnetic resonance to understand the dynamic response of these systems.

Keywords: *nanowires, microwave, broadband, ferromagnetic resonance.*

Introduction

Magnetic nanowires and their response at microwave frequencies is an interesting subject of study. The inherent shape anisotropy and tunable collective response of nanowires leads to the properties which can be exploited to fabricate a class of microwave devices such as circulators, isolators and tunable filters [1, 2] New generation microwave devices must be of smaller dimension, because of the growing demand of compact products. Present microwave device elements are still made of bulk ferrite materials which make the device bigger and less efficient. High frequency devices fabricated from magnetic nanostructures has a great future, but has a long way to go for practical applications.

The complete understanding of physics and the ways to exploit magnetic nanostructured material is still to be developed. Fabrication processes must be controlled so that it can be implemented on large volume productions. It is to be noted, magnetic nanostructures grown in random orientations have less significance because they will give an average response which is not much different from bulk magnetic materials in contrst nanowires grown parallel to each other show promising results in device application. Template based synthesis of nanomaterials was pioneered by Martin[3, 4]

In a nut shell Complete understanding of underlying physics (to predict the behavior of the nanostructures), fabrication processes of nanostructures showing desirable magnetic properties, measurement and analysis of the responses, development of measurement techniques in terms of repeatability, and ease of use are the main pillars of inventing and bringing new devices in the market

In this thesis we have described fabrication processes of Nickel nanowires in alumina template and possible method to measure the length of nanowire by alternate method (by saturation magnetization values) which may be a faster method to determine length of nanowires in contrast to SEM which requires sample preparation and is a time taking process.

We studied two types of magnetic systems: first one was the system of complex array of Nickel Nanowires grown in homemade AAO template provided by Prof. Wiley's group. The system was consists of Nanowires of different interwire distance and diameters in which we studied angular variation of ferromagnetic resonance at room temperature and at 4.2 K. The second system was a series of ferromagnetic-antiferromagnetic coupled multilayers having different strength of the exchange bias field. Here we studied effect of the exchange bias coupling on the X-Band and broad band ferromagnetic resonance of IrMn/NiFe multilayer thin film system. The multilayer samples were provided in collaboration with Dr. Garcia from MIT. These samples were produced by sputtering technique. Chapter wise organization of the thesis is as follows.

Chapter1, *Overview of magnetism,* gives a background about basic theory needed to understand the ferromagnetism and phenomena associated with them like Ferromagnetic resonance (FMR) and exchange bias.

Chapter 2, *electrodeposition of Nickel nanowires,* method of electrodeposition of Nickel nanowires in alumina template is discussed. Details of experimental setup and methods of determining growth rate is discussed.

Chapter 3, *microwave measurement techniques*, discusses briefly two measurement techniques viz. X-Band (9.8 GHz) and Broadband (50 MHz to 40 GHz) using Vector Network Analyzer. Subsequently results obtained from measurement using two types of waveguides were discussed with their advantages and disadvantages.

Chapter 4, *broadband and X-Band FMR of ordered Nickel nanowire,* represents X-Band (9.8 GHz) measurement done on complex Nickel nanowire arrays at room temperature and at 4.4 K, the dynamic results were correlated with information obtained from First Order Reversal Curve (FORC).

Chapter 5, *ferromagnetic resonance of exchange biased multilayer system,* the results obtained from broadband measurement and X-Band measurement has been discussed. The microwave measurement results have been correlated with the First Order reversal Curve (FORC).

Chapter1 Overview of Magnetism

This thesis deals mainly with the study of magnetic properties of materials with ferromagnetic order. In this chapter we will review several concepts necessary for the description and understanding of the results we obtained and will be presented in the subsequent chapters.

1.1 Ferromagnetism

The origin of magnetism is the existence of magnetic moments at the atomic level, mainly because of the spin of electron. These atomic magnetic moments in a ferromagnetic material align in one direction due to exchange interaction between nearby spins. This type of interaction gives rise to a net magnetization in the system called spontaneous magnetization.

But magnetostatic energy or self energy which originates from shape of the sample, tries to get the lowest possible energy by reducing the sample in smaller regions of net magnetization called domains (fig1.1)

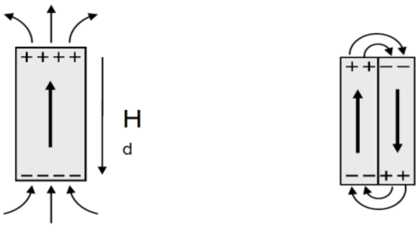

Fig 1.1: Reduction of total energy by formation of domains

If we keep on reducing the dimension of a ferromagnetic material, below a certain size it will become a single domain particle. The critical size for a particular material is dependent on several contributions to the total magnetic free energy of the specimen; mainly exchange energy which keeps the spins aligned parallel to each other and magnetocrystalline anisotropy energy, which is responsible for the preference of the magnetization to be oriented along a certain direction. In the following subsection a short review of the different magnetic free energy contribution will be provided.

1.2 Anisotropy energy

The orientation of the magnetization, i.e. the existence of easy and hard axis directions of magnetization in a crystal is due to several types of anistropy energy originated from various factors discussed in this section.

1.2.1 Magnetocrystalline energy

The magnetocrystalline anisotropy defines the tendency of magnetization to be aligned along a crystallographic direction. In a uniaxial material, the magnetocrystalline energy density can be expressed as

$$\mathrm{K_c = K_0 + K_1 Sin^2\theta + K_2 Sin^4\theta + \ldots}$$

where $\mathrm{K_0}$, $\mathrm{K_1}$, $\mathrm{K_2}$ ($\mathrm{K_1 > K_2}$) are anisotropy constants and θ is the angle between the magnetization direction and the easy axis of the crystal. $\mathrm{K_0}$ is usually neglected because it is independent of magnetization direction. Where, The anisotropy constants are usually of the order of 10^6 erg/cc.

1.2.2 Shape anisotropy

Shape anisotropy is associated with the magnetostatic energy which originates from the “free pole” existing at the end surface. As an example in rod-like specimens there will be a preferred axis along the long dimension because the demagnetizing energy is much less in this direction than it would be in the short dimension of the specimen. In a single prolate ellipsoidal particle, the magnetostatic energy density can be given in the following way.

$$\mu_{ms} = +\frac{\mu_0\, M_s^2}{2}\Delta N \mathrm{Cos}^2\theta + \mathrm{Const}$$

Where θ is the angle between the magnetic field vector and magnetization vector. ΔN is called the effective demagnetization factor which is the difference between two demagnetization factors. One is along the easy axis of the particle and the other is perpendicular to the easy axis.

1.2.3 Magnetoelastic energy

The magnetoelastic energy or magnetostrictive energy results from the interaction between the magnetization and the mechanical strain of the lattice. The energy is stored as either a distortion or stress in the crystal. The magnetoelastic energy is defined as zero in an unstrained lattice.

1.2.4 Zeeman energy

Zeeman energy is the potential energy of a magnetized body in an external magnetic field. In SI units, it is given by

$$E_{zeeman} = -\mu \int M.H_{ext} dV$$

Where H_{ext} is the external field and M is the local magnetization, and the integral is done over the volume of the body.

1.3 Exchange energy and exchange bias

The origin of this energy is quantum mechanical exchange integral which is consequence of Pauli's exclusion principle. The exchange interaction is isotropic i.e. it is independent of the direction. Exchange energy can be expressed as

$$\mathrm{W_{ex}} = -2\mathrm{JS}^2\Sigma\mathrm{Cos}\emptyset_{\mathrm{ij}}$$

Where

J = exchange integral between neighboring spins

S = net spin angular momentum of atom

$\emptyset_{\mathrm{ij}}$ = angle between direction of spin momentum vectors of atoms i and j.

It is usually assumed that the angle ϕ between neighboring spins is small; so replacing the cosine term with first two terms of its Taylor series, the part of the energy which varies with the angle is given by

$$\Delta\mathrm{W_{ex}} = \mathrm{JS}^2 \sum \emptyset_{\mathrm{ij}}^2$$

One of the consequences of exchange energy is exchanged bias which is observed in Ferromagnetic (FM)/Antiferromagnetic (AF) bilayer. In this type of system spins at the surface of antiferromagnetic layer is aligned in the direction of magnetic field (parallel to the film plane) which is present during sputtering process.This type of systems shows .an equivalent "unidirectional" anisotropy with anisotropy energy of the form:

$$\mathrm{W_E} = -\mathrm{K_E}\cos\theta$$

Where θ is the angle between the magnetization direction in the ferromagnet and the preferred direction of the exchange anisotropy.

The hysteresis loop of exchange biased system shows offset from zero applied magnetic fields which is defined as exchange bias field. Another consequence of exchange coupling is the increased coercivity of ferromagnetic layer (Fig 1.3a). The exchange biasing effect can be used to control the magnetization in devices such as spin valves. The magnetization of one FM layer is fixed by exchange biasing effect, while other FM layer rotates freely in an applied magnetic field

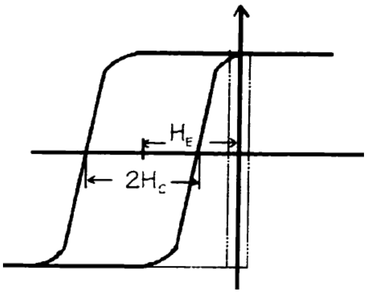

Fig 1.3a: Hysteresis loop shift and enhancement of the coercivity due to exchange bias.

1.4 Stoner Wohlfarth model

Stoner and Wolhfarth proposed a magnetization reversal mode for a single domain particle in 1948[5].

His model was based on following assumptions:

- Particles are small enough to be single domains and the exchange energy holds all spins tightly parallel to each other. So it is assumed that the rotation of magnetization is coherent.
- Magnetic interactions between particles are neglected.

- Thermal relaxation effects are neglected

For a particle with uniaxial anisotropy in an external magnetic field (Fig 1.4a), the total energy density of this system can be mathematically written as

$$E = KSin^2\theta - \vec{M}.\vec{H}$$

$$= KSin^2\theta - M(H_x Sin\theta + H_z Cos\theta)$$

The dependence of M on H is given by the equilibrium condition

$$\frac{dE}{d\theta} = 0 \text{ and } \frac{\partial^2}{\partial\theta^2} > 0$$

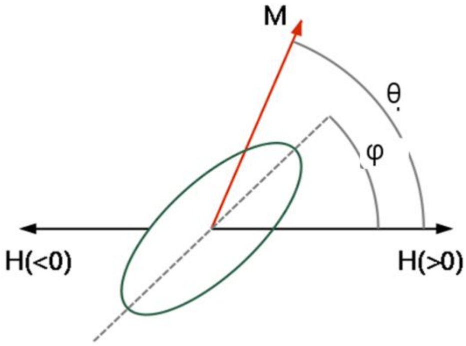

Fig 1.4a: A particle with uniaxial anisotropy in applied field H

It is also deduced that the switching field, at which the metastable state become unstable and the magnetization switches to the nearest minimum, satisfies the following equation

$$H_x^{2/3} + H_z^{2/3} = \left(\frac{2K}{M}\right)^{2/3}$$

It represents a closed astroid curve as shown in the Fig1.4b

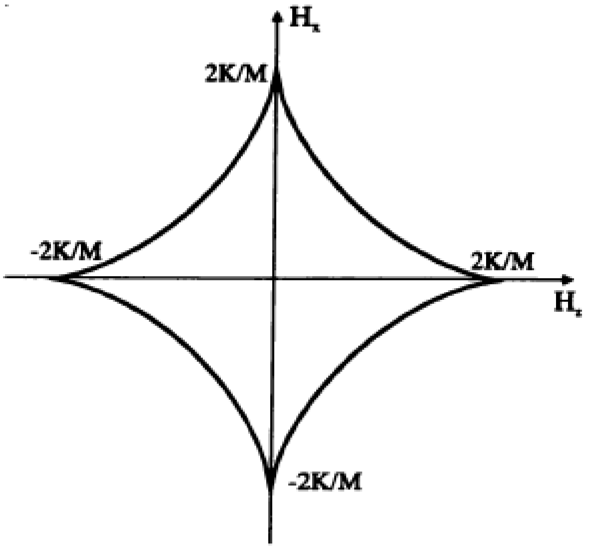

Fig 1.4b: Switching field in the stoner-Wolfarth model shows a closed astroid curve in the H_x, H_z plane

At a critical angle θ_c=0 and ϕ=0 zero one gets a rectangular hysteresis loop as shown in fig 1.2.5c. At φ=90^o the magnetization M is a linear function of H showing no hysteresis with $\mathrm{M/M_s} = \mathrm{m}$, the normalized magnetization

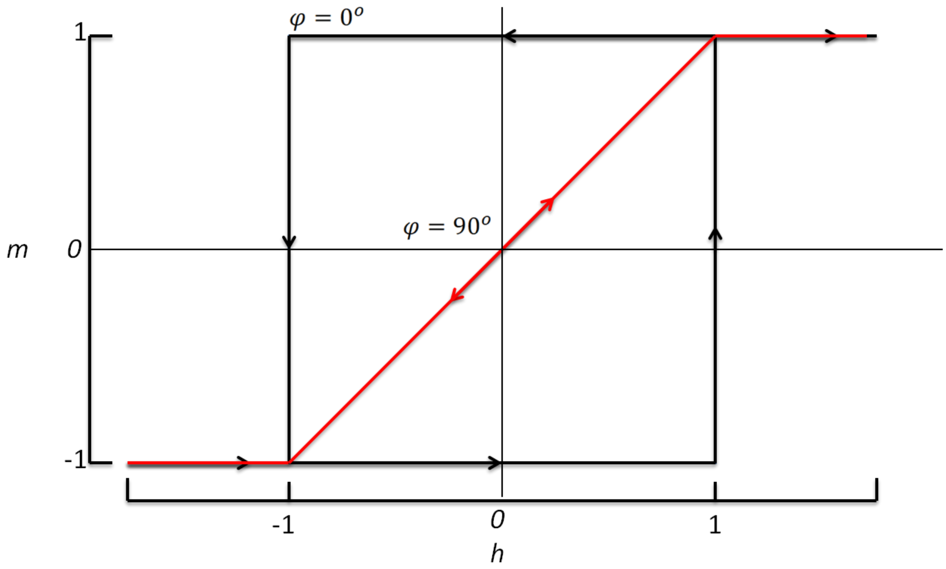

Fig 1.4c: Magnetization loop of a single domain particle. Here m (=M/M_s) and h (=H/H_k) are the normalized magnetization and normalized field.

1.5 Neel Brown model

Stoner Wohlfarth model can be applied in an idealized systems which are non interacting and with no thermal excitation, but it fails when the model is applied to a system at non zero temperature. In case of ideal single domain particle on thermal excitation, the moment tends to decay exponentially toward thermal equilibrium [6]. The theory of thermal relaxation was first proposed by Néel[7] and later developed by Brown [8].

The Néel-Brown model gives the time $\tau = \tau_0 e^{\frac{KV}{K_B T}}$, for an ideal particle to spontaneously switch its magnetization by overcoming the anisotropy energy barrier $\Delta E = KV$, where K is the anisotropy constant, V is the volume of the particle at a given temperature$T$ and K_B is Boltzmann constant, typically $\tau_0 = 10^{-9}$s.

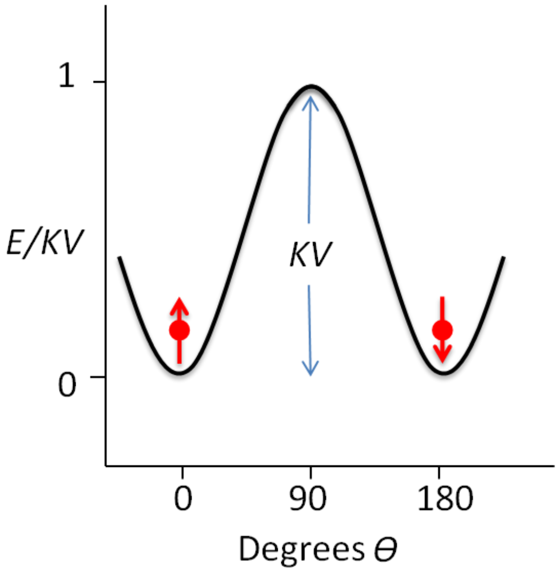

Fig 1.5a: Two equilibrium conditions (minimum local energy) of a system separated by energy barrier KV

The magnetic behavior of the system is strongly dependent on the measurement time τ_m. If $\tau_m \gg \tau$ then the thermal relaxation is very fast and the energy barrier is overcome easily, in this case the system exhibits Superparamagnetic behavior (red curve in figure 1.5b). If $\tau_m \ll \tau$ then the relaxation time is slower and the system is stable exhibiting ferromagnetic behavior (blue curve in figure 1.5b). The temperature that separates the Superparamagnetic regime and blocking one is called the blocking temperature T_B [9].

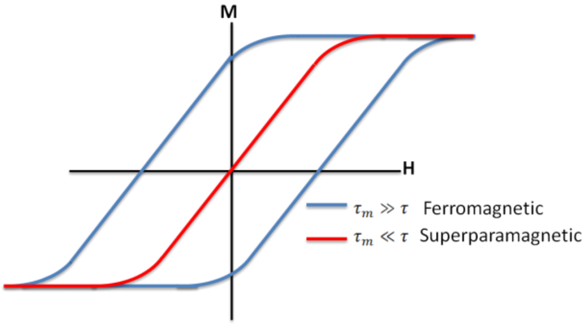

Figure 1.5b: M-H curve of Ferromagnetic (Blue) and Superparamagnetic (Red) samples. A superparamagnetic material shows no hysteresis.

1.6 Landau-Lifshitz-Gilbert (LLG) equation

Landau Lifshitz developed a phenomenological theory for the dynamics of magnetization in ferromagnetic materials which are kept in external magnetic field. Besides the expected precession term a relaxation term was introduced in the equation of motion which leads to the equation.

$$\dot{\mathrm{M}} = -\gamma[\mathrm{M} \times \mathrm{H}_{\mathrm{eff}}] - \frac{\lambda}{\mathrm{M}^2}[\mathrm{M} \times \mathrm{M} \times \mathrm{H}]$$

Where λ (stands for the relaxation frequency) characterizes the dipole dipole interaction between the elementary magnetic moments. Above equation is sometimes written in the form

$$\dot{\mathrm{M}} = -\gamma[\mathrm{M} \times \mathrm{H}_{\mathrm{eff}}] - \alpha\frac{\gamma}{\mathrm{M}}[\mathrm{M} \times \mathrm{M} \times \mathrm{H}]$$

The relaxation can physically be realized as if magnetization vector moves along the spiral and gradually approaches the equilibrium position see fig1.6a

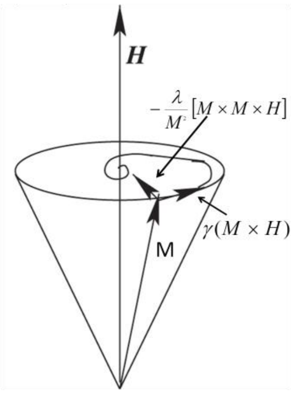

Fig 1.6a: Damped precession of magnetic moment M in applied magnetic field H

In 1955 Gilbert replaced the damping term in the Landau-Lifshitz (LL) equation by one that depends on the time dependence of the magnetic field

$$\dot{\mathrm{M}} = -\gamma^*[\mathrm{M} \times \mathrm{H}_{\mathrm{eff}}] + \frac{\alpha_0}{\mathrm{M}}[\mathrm{M} \times \dot{\mathrm{M}}] \quad 1.3.2a$$

Where $\gamma^* > 0$ and $\alpha_0 > 0$

So in contrast to Landau Lifshitz equation the relaxation term in LLG equation is proportional to the rate of change of the magnetization in time.

1.7 Ferromagnetic resonance

Ferromagnetic resonance was unknowingly discovered by V. K. Arkad'yev when he observed the absorption of UHF radiation by ferromagnetic materials in 1911. He observed that a ferromagnetic material when put in external magnetic field absorbs radiation strongly at a particular frequency called resonance frequency. A qualitative explanation of FMR was offered up by Ya. G. Dorfman in 1923. He suggested that FMR is fundamentally identical to optical transitions due to Zeeman effect.

1.8 Ferromagnetic resonance in magnetic nanowires

Ferromagnetic resonance technique is one of the best characterization techniques for magnetic Nanowires array as it can give information about the average magnetic anisotropy of the system. It can also give some ideas about relaxation mechanism and elementary excitations. Anisotropy field can be measured directly from the FMR. According to the Smit Beljers dispersion relation[10, 11]

$$\left(\frac{\omega}{\gamma}\right)^2 = \frac{\left(E_{\theta\theta}E_{\varphi\varphi} - E_{\theta\varphi}^2\right)}{(M_S \mathrm{Sin}\theta)^2}\Bigg|_{\theta=\theta_0,\varphi=\varphi_0} \qquad 1.8a$$

where ω is the microwave frequency, γ is the gyromagnetic factor, M_s is the saturation magnetization, $E_{\theta\theta}$, $E_{\varphi\varphi}$, and $E_{\theta\varphi}$ are the second derivative of the free energy (E) with respect to the spherical angles (θ, φ) at equilibrium direction. The equilibrium direction can be determined by first derivative of free energy by zero i.e. E_θ=0 and E_φ=0

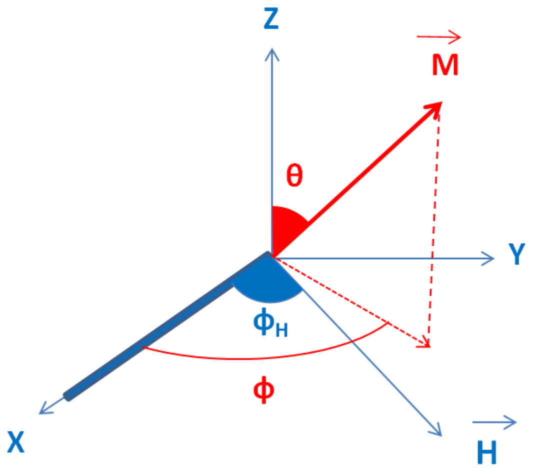

Fig 1.8a: defining coordinate axis where NW axis coincides with X axis. Magnetic field is sweeping in XY plane.

We can assume the Nanowires as a system of uniaxial anisotropy due to its shape. Let us assume second order uniaxial anisotropy described by the free energy per unit volume

$$E = -M_s H \mathrm{Sin}\theta \mathrm{Cos}(\varphi - \varphi_H) - K\mathrm{Sin}^2\theta\mathrm{Cos}^2\varphi \qquad 1.8b$$

Here H is external magnetic field applied in the XY plane, M_s and K are saturation magnetization and anisotropy energy respectively. φ is angle between magnetization and X axis

For equilibrium value of θ we equate first derivative of E see eqn 1.8b

So

$$E_\theta = 0 \;\Rightarrow [-H\mathrm{Cos}(\varphi - \varphi_h) + \;K(\mathrm{Sin}^2\varphi - 1)\mathrm{Sin}\varphi]\mathrm{Cos}\theta = 0 \qquad 1.8c$$

This gives $\theta_0 = \frac{\pi}{2}$

Using eqn 1.8a and 1.8b at $\theta_0 = \frac{\pi}{2}$ we obtain the following dispersion relation

$$\left(\frac{\omega}{\gamma}\right)^2 |_{\theta_0} \;=\; [H\mathrm{Cos}(\varphi - \varphi_h) + H_A(\mathrm{Cos}^2\varphi)][H\mathrm{Cos}(\varphi - \varphi_h) + \;H_A\mathrm{Cos}2\varphi] \qquad 1.8d$$

Case1: H // to the wire and H_A>0

$$\frac{\omega}{\gamma} = H + H_A \qquad 1.8e$$

Case2: H// to the wire and H_A<0

$$\frac{\omega}{\gamma} = H_A - H \qquad 1.8f$$

Case3: $H_\perp$ easy axis and H<H_A

$$\left(\frac{\omega}{\gamma}\right)^2 = (H_A^2 - H^2) \qquad 1.8g$$

Case4: $H_\perp$ easy axis, H>H_A.>0

$$\left(\frac{\omega}{\gamma}\right)^2 = H(H - H_A) \qquad 1.8h$$

From case 1

$$\left(\frac{\omega}{\gamma}\right)_{\parallel} = \mathrm{H} + \mathrm{H_A}$$

From case4

$$\left(\frac{\omega}{\gamma}\right)_{\perp}^{2} = \mathrm{H(H - H_A)}$$

$$\Rightarrow \left(\frac{\omega}{\gamma}\right)_{\perp} = \mathrm{H}\sqrt{1 - \frac{\mathrm{H_A}}{\mathrm{H}}}$$

$$\sim \mathrm{H}\left(1 - \frac{\mathrm{H_A}}{2\mathrm{H}}\right)$$

So

$$(\mathrm{H})_{\parallel} = \frac{\omega}{\gamma} - \mathrm{H_A}$$

and

$$(\mathrm{H})_{\perp} = \frac{\omega}{\gamma} + \frac{1}{2}\mathrm{H_A}$$

So from above two equations we get

$$\mathrm{H_\perp - H_\parallel} = \tfrac{3}{2}\mathrm{H_A} \qquad 1.8\mathrm{i}$$

Therefore from the values of resonance field in two directions (parallel and perpendicular to the easy axis) gives the information about anisotropy field.

Chapter 2 Electrodeposition of Nickel Nanowire

Electrodeposition of Nanowires using alumina template is one of the most versatile methods of preparing periodic array of Nanowires. The method is simple and does not require sophisticated instrumentation like electron beam lithography. Anodic porous alumina and track etched polymer membranes are the most common nanoporous materials for growing Nanowires [4, 12]

We have grown Nickel Nanowires first in commercial AAO templates and determined the growth rate. To quantify the effect of interactions one needs both a suitable method to experimentally vary the strength of interactions in arrays of magnetic Nanowires and a method to measure the effect of the interactions. Therefore accurate value of growth rate is required for good control on the length of Nanowires. In this chapter we described how we estimated the growth rate from theory of electrodeposition and how we measured the growth rate directly (from SEM) and indirectly (from saturation magnetization).

2.1 Electrodeposition technique

Nickel Nanowires were grown by electrodeposition method using two different quality of templates: commercial nanopore inorganic alumina (Anodisc #25 from Whatman) and homemade anodized alumina membrane. The process was developed using DC electrodeposition method in galvanostatic (constant current) mode, using a Teflon bath cell. For electrolyte, a commercial high-purity of Nickel sulphamate ($NiSO_4 . 7H_2O$ from TECHNIC NC). Alumina template (one side sputtered with 200 nm film of copper), which acts as cathode. A Platinum wire of high-purity (99.99%) was used as Anode. To avoid inhomogeneity in the solution during the deposition process, the solution was stirred with magnetic stirrer during deposition with 300 RPM. The temperature (22 ^{0}C) and stirring was controlled using IKA control-Visc. Figure 3.1a shows photograph of the electrodeposition set up. Fig 2.1b and 2.1c shows top view of electrodeposition cell and schematic representation of the electrodeposition process. For consistent quality of sample constant pH (3-4) should be maintained for which purpose Boric acid is mixed to the solution

As the deposition current was kept constant the voltage was also constant near to 3.2 V throughout the deposition process. Fig2.1d shows typical voltage vs time graph where we can see the voltage is pretty much constant after an initial ramp.

We measured the porosity of the alumina template by analyzing the SEM images (fig2.2.3a) using imageJ software[13]. Mean pore diameter was calculated as 297 nm, template thickness was 60 um and porosity came out to be 0.41. These values were needed for a first estimation of the growth rate by applying Faraday's law of electrolysis discussed later in the chapter.

Basically we theoretically estimated the length of Nanowires by using Faraday's law of electrolysis and then verify it indirectly from the data obtained from magnetization and then measured directly from the SEM. The growth rate (µm/min) was found to be constant (linear dependence of the Nanowire length vs. time) in all the three methods. However, but we found that the growth rate predicted by theoretical estimation was larger than the ones obtained from magnetization and microscopy measurements. This fact is not unexpected because theoretical calculation did not consider other processes going on in parallel with reduction of Ni (like electrolysis of water). We also found that the growth rate estimated from magnetization measurements came out to be larger than that from direct length measurements this may be because we used bulk density of Nickel for the estimation which may not be exactly same for the Nanowires (fig2.2.3c). Table2.1 has consolidated the information about the sample series used to find out the growth rate.

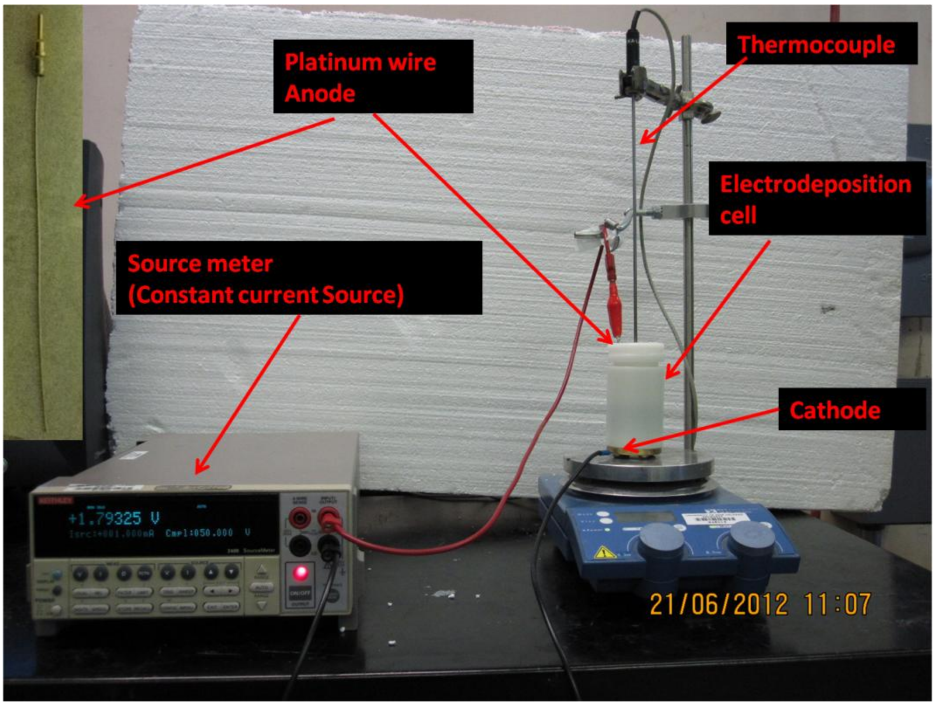

Figure 2.1a: Front view of the Electrodeposition Set up.

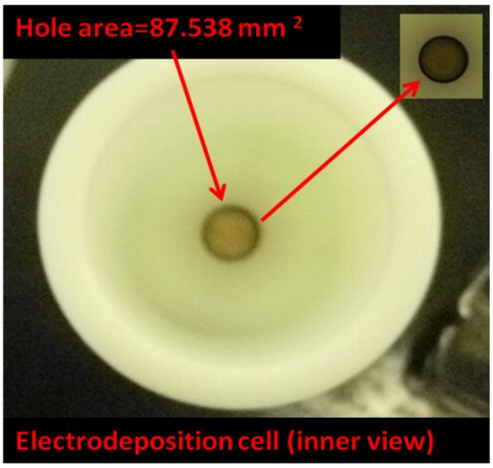

Figure 2.1b: Top view of the Teflon bath cell. The hole is at the bottom of the cell. The AAO template was fixed at the bottom hole

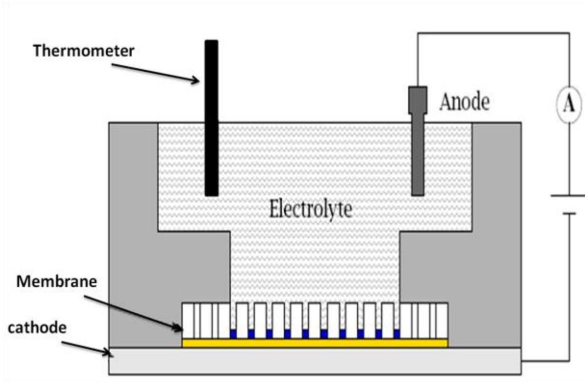

Figure 2 1c: Schematic representation of the electrodeposition process of metallic Ni on the surface of the cathode template

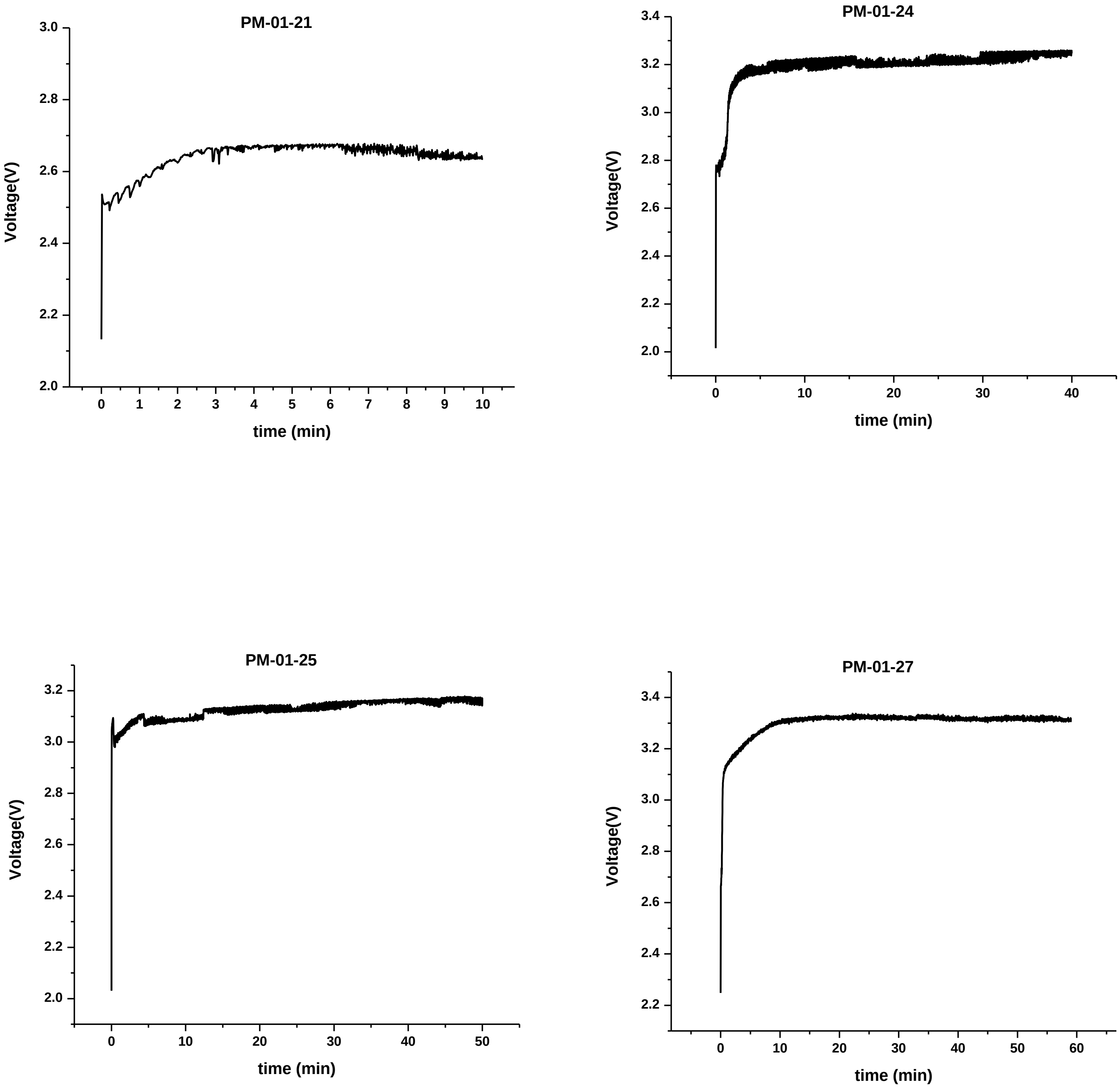

Fig 2.1d: Typical Voltage Vs time curve for the set of sample with different growth time

Table 2.1 sample details with deposition time and length

Sample #	Deposition time (min)	Ms (emu/cm2)	Length (from SEM) (um)	Length (estimated from M_s (um)	Aspect ratio
PM-01-21	**10**	**0.0723**	**2.8**	**3.6**	**56**
PM-01-22	**20**	**0.154**	**5.6**	**7.7**	**46**
PM-01-23	**30**	**0.237**	**8.4**	**11.9**	**37.3**
PM-01-24	**40**	**0.318**	**11.2**	**15.9**	**28**
PM-01-25	**50**	**0.367**	**14.0**	**18.4**	**18.6**
PM-01-27	**60**	**0.460**	**16.8**	**23.1**	**9.3**

2.2 Estimation of growth rate

We have used three methods for estimation of growth rate. First one is calculated theoretically from Faraday’s law of electrolysis which gives the preliminary idea of growth rate (discussed in section2.2.1). But this method is not accurate because the real growth rate may differ largely from the predicted one as several factors which affect the growth rate (like temperature, pH, current etc.). The second method is estimating the growth rate from the value of saturation magnetization which gives relatively better estimation of growth rate (discussed in section 2.2.2) and the third method is direct measurement from Scaning Electron Microscopy (SEM) observations.

2.2.1Estimation of growth rate from Faraday’s law of electrolysis

To estimate the growth rate we followed Faraday’s law of electrolysis.

Faraday’s First law:

The mass of a substance deposited at an electrode during electrolysis is directly proportional to the quantity of electricity transferred at that electrode. Quantity of electricity refers to the quantity of electrical charge, typically measured in Coulomb.

Faraday’s second law:

For a given quantity of electricity (electric charge), the mass of an elemental material deposited at an electrode is directly proportional to the element's equivalent weight. The equivalent weight of a substance is its molar mass divided by an integer that depends on the reaction undergone by the material.

So mathematically

$$\mathrm{m} = \left(\frac{\mathrm{Q}}{\mathrm{F}}\right)\left(\frac{\mathrm{M}}{\mathrm{n}}\right)$$

Where

- m is the mass of the substance liberated at an electrode in grams
- Q is the total electric charge passed through the substance
- F = 96,485 C mol^{-1} is the Faraday constant
- M is the molar mass of the substance
- n is the valency number of ions of the substance (electrons transferred per ion).

Now Q = It, where I is the current (C sec^{-1}) and t is the time of deposition

We have

$$\mathrm{m} = \left(\frac{\mathrm{It}}{\mathrm{F}}\right)\left(\frac{\mathrm{M}}{\mathrm{n}}\right) \qquad 3.2.1\mathrm{b}$$

$$\text{or} \quad \rho\mathrm{V} = \left(\frac{\mathrm{It}}{\mathrm{F}}\right)\left(\frac{\mathrm{M}}{\mathrm{n}}\right) \qquad 2.2.1\mathrm{c}$$

Where ρ is the density of material to be deposited and V is the volume of the material deposited

In our case deposited volume is given by:

$\mathrm{V} = \mathrm{LPA}$ Where L is the length of the Nanowire, P is the porosity of the template and A is the area of the template used for electrodeposition. The membrane's porosity is defined as the ratio occupied by the pores, A_{pores} to the total area, A, i.e. $P=A_{pores}/A$.

So $\rho\mathrm{LPA} = \left(\frac{\mathrm{It}}{\mathrm{F}}\right)\left(\frac{\mathrm{M}}{\mathrm{n}}\right)$ or $\mathrm{L} = \left(\frac{\mathrm{ItM}}{\mathrm{Fn}\rho\mathrm{PA}}\right)$. Hence, the growth rate (r=L/t) of Nanowires can be estimated as

$$\mathbf{r} = \left(\frac{\mathbf{IM}}{\mathbf{Fn\rho PA}}\right) \qquad 2.2.1\mathrm{d}$$

One notes the linear dependence of the growth rate with the current, as expected.

2.2.2 Estimation of growth rate from saturation magnetization

The magnetization loops, M vs. H, were measured systematically on the electrodeposited sample membranes. Taking into account the full area of the sample (A), and porosity (P), the magnetization was normalized by the effective volume filled by the Ni Nanowires. Comparing this value with the expected saturation magnetization of metallic Ni (480 emu/cm3), the length of the Nanowire can be estimated as follows,

Let

$$(\mathbf{m_{sat}})_{\mathbf{exp}} = \frac{\mathbf{m_{max}}}{\mathbf{AxP}}\ \mathbf{emu/cm^2} \qquad 2.2.2\mathrm{a}$$

here

$(\mathrm{m_{sat}})_{\mathrm{exp}}$ = Saturation magnetic moment per unit area of the sample (template) used for measurement

$\mathrm{m_{max}}$ = Maximum magnetic moment measured of the sample from MH loop

A= Area of the sample used for measurement

P= Porosity of the template

Now let us define $\mathrm{V_{eff}}$ as the effective volume of the Nickel deposited defined by

$$\mathbf{V_{eff}(cm^3) = Area(cm^2)\ \times P \times L(cm)} \qquad 2.2.2\mathrm{b}$$

Here L is the length of the Nanowire grown

So $(\mathrm{M_{sat}})_{\mathrm{exp}} = \frac{\mathrm{m_{max}}}{\mathrm{V_{eff}}} = \frac{\mathrm{m_{max}}}{\mathrm{Area\times P\times L}} = \frac{(\mathrm{m_{sat}})_{\mathrm{exp}}}{\mathrm{P\times L}}\ \mathrm{emu/cm^3}$ 2.2.2c

where $(\mathrm{m_{sat}})_{\mathrm{exp}}$ represents the magnetic moment per unit area of the deposited template.

Comparing saturation magnetization of measured value with the standard value that is 480 emu/cm^3

$$(\mathrm{M_{sat}})_{\mathrm{exp}} = 480\ \mathrm{emu/cm^3}$$

Or $\frac{(\mathrm{m_{sat}})_{\mathrm{exp}}}{\mathrm{P\times L}} = 480\ \mathrm{emu/cm^3}$

$$\mathrm{L(cm)} = \frac{(\mathrm{m_{sat}})_{\mathrm{exp}}}{\mathrm{P\times 480}}$$

Or $\mathbf{L(\mu m)} = \frac{(\mathbf{m_{sat}})_{\mathbf{exp}}}{\mathbf{P\times 480}} \times \mathbf{10^4}$ 2.2.2d

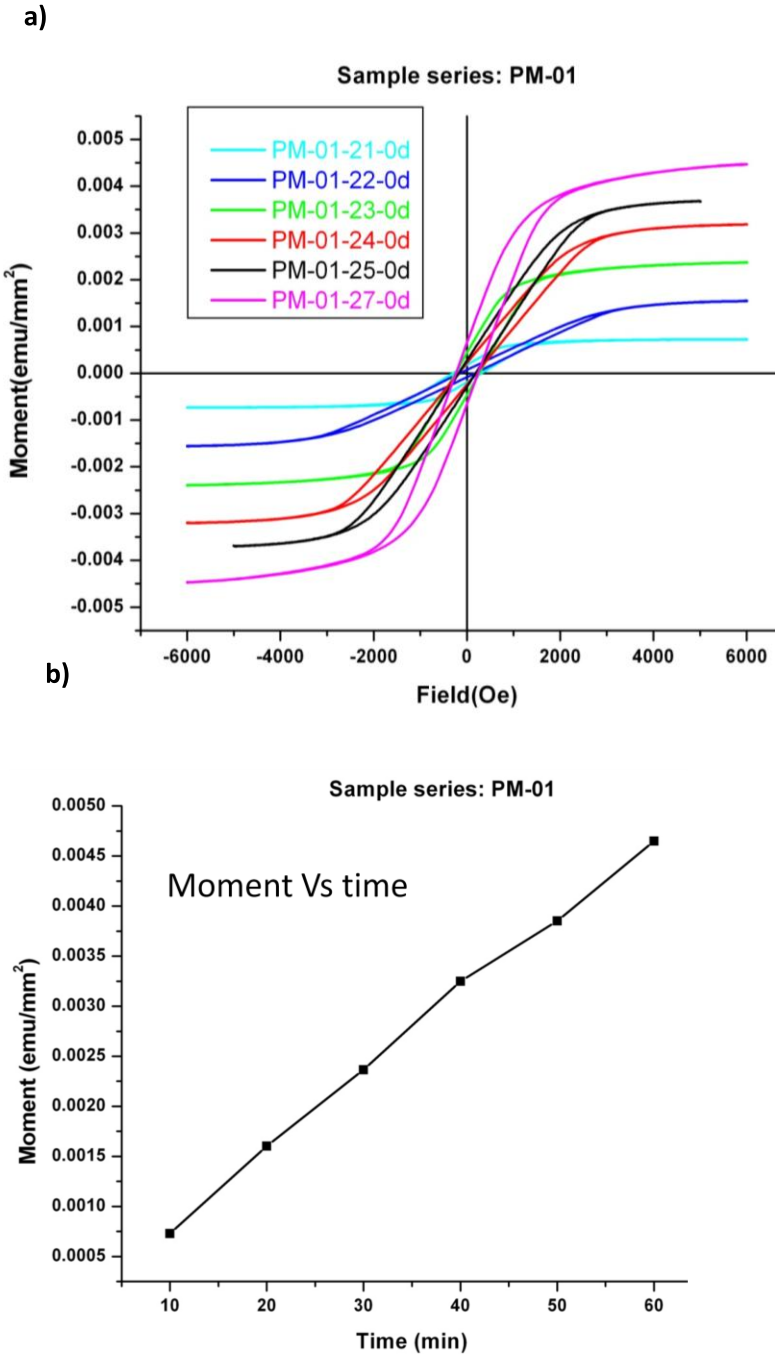

Fig2.2.2 a): M-H loop of the sample series; b) Saturation magnetic moment per unit area vs deposition time of the sample series.

2.2.3 Estimation of growth rate from SEM

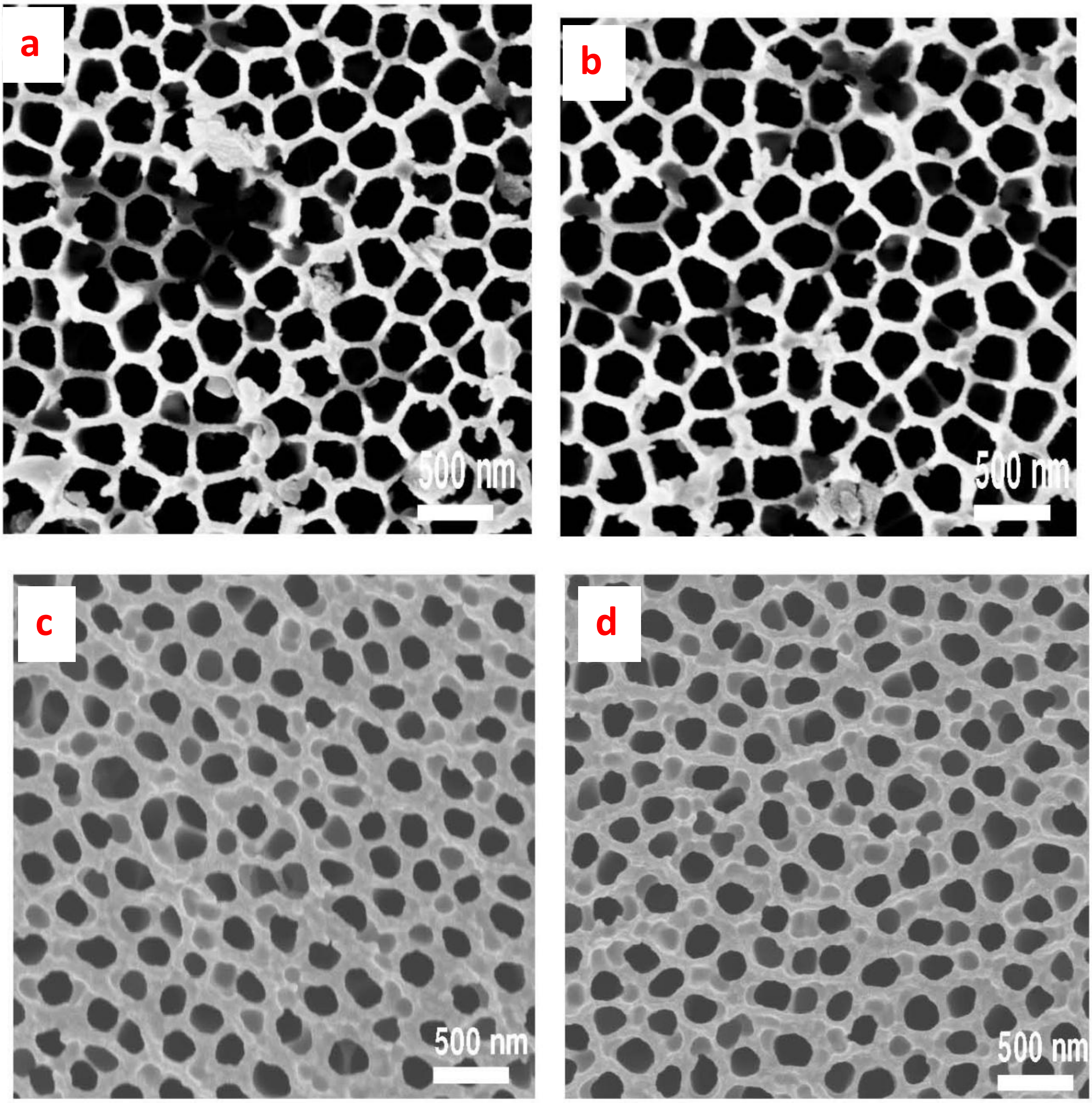

Fig 2.2.3a: SEM Images before deposition [a), b)] and after deposition [c), d)] Mean pore diameter is 297 nm, template thickness is 60 um and porosity is 0.41

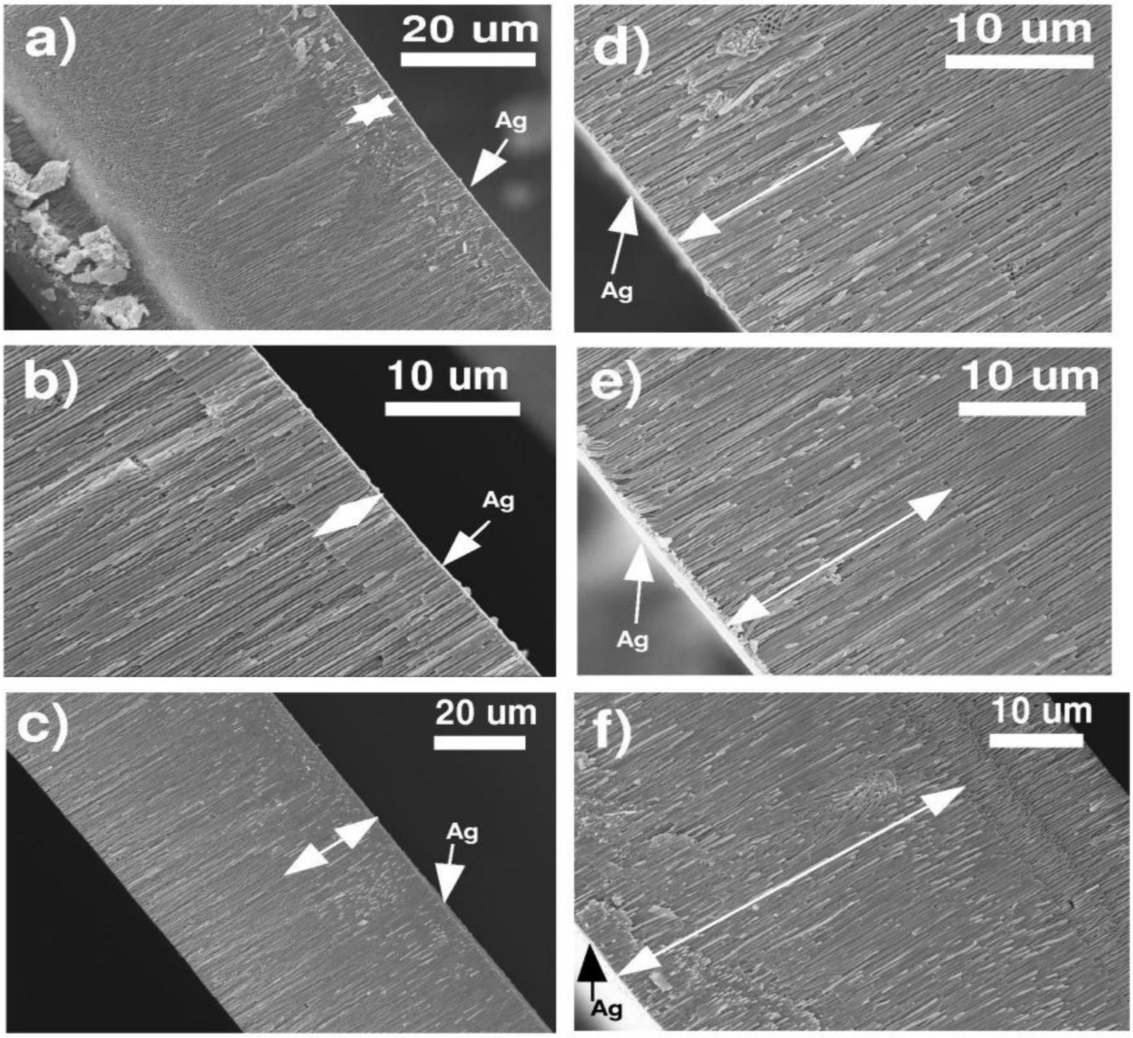

Fig 2.2.3b: Length measurement of Nanowires by SEM
a)PM-21 (2.8 um); b) PM-22 (5.6 um) ; c) PM-23 (8.4 um);
d) PM-24 (11.2 um) ; e) PM-25 (14.0 um); f) PM-27 (16.8 um)

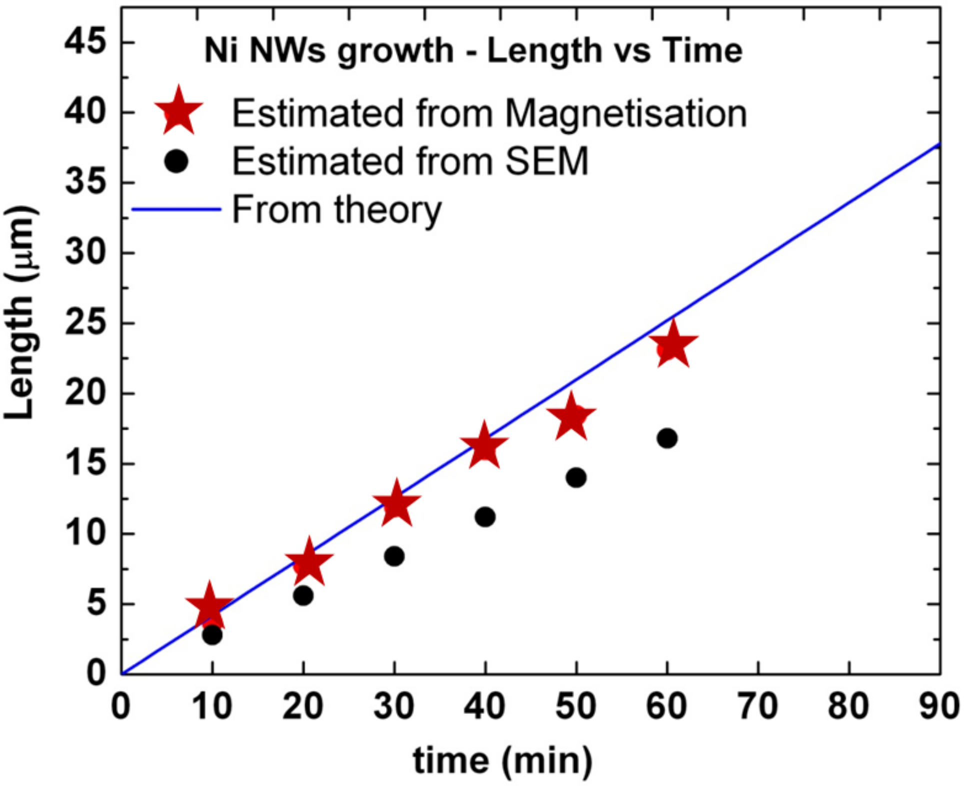

Fig 2.2.3c: Comparison of Growth rates obtained from theory, from saturation magnetization data and direct measurement from SEM.

2.3 Magnetization loop of Nickel nanowires of varying length

We have grown another series of Nanowires in alumina commercial template with different deposition time with constant current (1 mA.). Magnetizations of these samples were measured at room temperature. It was seen that as the length of Nanowires increases the easy axis switches from perpendicular to the Nanowires to parallel to the Nanowires as studied by Trusca etal and others [14-16].Figure 2.3a shows the M-H loop of Nanowires with increasing length. Table 2.3 summarizes current, time of deposition, and length of the Nanowires produced.

Table 2.3: Sample details with deposition parameter

Sample	Current	Time	Length
PM_01_41	1mA	18 min	1 µm
PM_01_40	1mA	35 min	2 µm
PM_01_42	1mA	53 min	3 µm
PM_01_43	1mA	88 min	5 µm
PM_01_45	1mA	178 min	10 µm

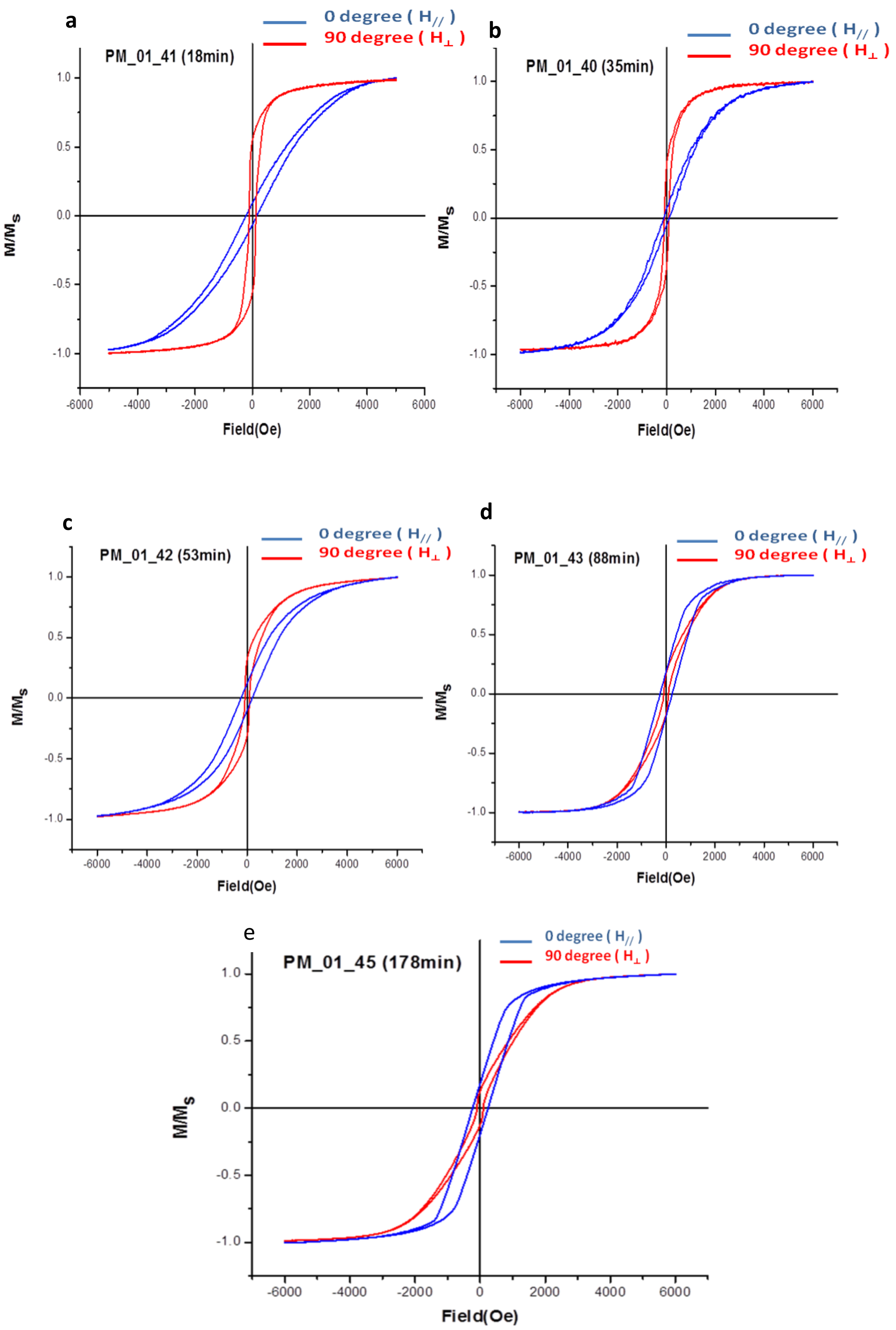

Fig 2.3a: Magnetization loop of Nickel Nanowires with increasing length from a) to e). The blue curve corresponds to the field applied along the axis of Nanowires

Chapter 3 Microwave measurement techniques

3.1 Introduction

The technological application of electromagnetic materials needs fundamental understanding of why those materials behave as they do. The electromagnetic properties of magnetic materials have not been fully understood this is the reason why magneto-electronics is still under development.

As the clock speeds of the electronic devices is approaching microwave frequencies it is more important to study materials behavior at these frequencies.

Magnetic Nanowire arrays are very interesting structures to be used at microwave frequencies because at these frequencies the wires's diameters is much smaller than the skin depth and the absorption of the electromagnetic field is very effective. Thus, through the phenomenon of ferromagnetic resonance (FMR) mentioned in chapter 1 it is possible to design microwave devices based on arrays of magnetic Nanowires.

In our study we used two different approaches to study the ferromagnetic resonance in magnetic Nanowire arrays. The first method is based on using a standard Electron paramagnetic Resonance (EPR) using a X-band (9.5 GHz) resonant cavity from Bruker (model EMX). The second method is based on using a Vector Network Analyzer (VNA) for generating a broadband microwave electromagnet field and a transmission line coupled with the specimen under study. In the following we briefly described these two methods.

3.2 X-Band Microwave measurement

EPR is a technique based on the absorption of electromagnetic radiation by the unpaired electrons in a sample which is usually in the microwave frequency region. The first EPR experiment was performed by E. K. Zavoisky in 1945. In optical spectroscopy Zeeman effect was a well known phenomena, but first EPR was observed after the development of radar during world war II. After World War II scientists got access to required components for the development of EPR. EPR has a broad range of applications in the field of physics, chemistry, biology, earth sciences, material sciences and medical field. In the case of ferromagnetic materials, as described in chapter 1 we have a similar absorption of electromagnetic energy called ferromagnetic resonance. In essence, an EPR spectrometer can be used for FMR investigations of magnetic materials

Spectrometer

In its simplest form an EPR spectrometer (Fig3.2b) consist of:

1. A monochromatic microwave source
2. A waveguide for guiding the microwave to the sample
3. A cavity for proper coupling between sample and the incoming waves
4. A detector to detect the response of a sample

Detector

The detector is a solid state diode sensitive to the microwave energy. In a typical spectrometer the static magnetic field B is modulated by an ac field of few KHz which helps in increasing S/N ratio. It is achieved by placing a Helmholtz coil on each side of the cavity along the axis of static magnetic field. The disadvantage of this method is distortion in line shape. The resulting signal is the first derivative of the absorption line in the limiting case. The shape of the absorption line is fitted to a mathematical function (e.g. Gaussian or Lorentzian).

Source

The frequency of incident energy is generally 9.5 GHz(X-Band). The microwave source is a Klystron. Now the most commonly used microwave sources in modern spectrometer are stabilized Gunn oscillators operating at fixed frequency which has less phase noise compared to klystron.

Resonator

It is a resonant cavity in which microwave enters through an iris. Frequency of the source is tuned to the resonance frequency of the cavity. The most desirable mode is the one which maximizes microwave magnetic field at the sample. The resonance cavity provided by Bruker has a maximum magnetic field of radiation at the centre (Fig3.2a)

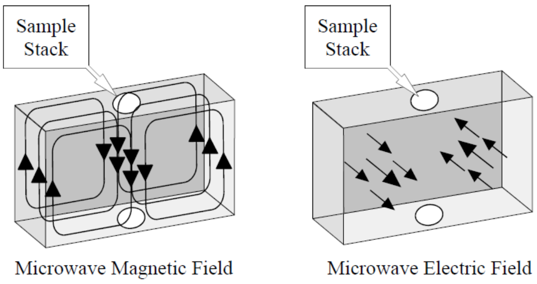

Fig 3.2a: Magnetic and electric field distribution in a standard EPR cavity

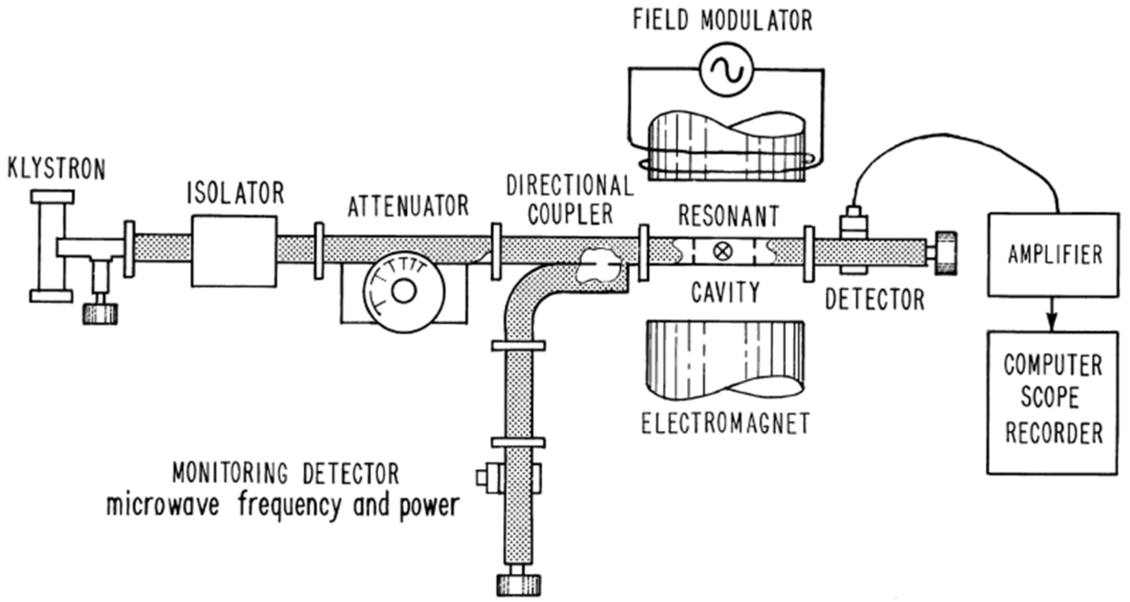

Fig 3.2b: A block diagram of an electron paramagnetic resonance (EPR) spectrometer

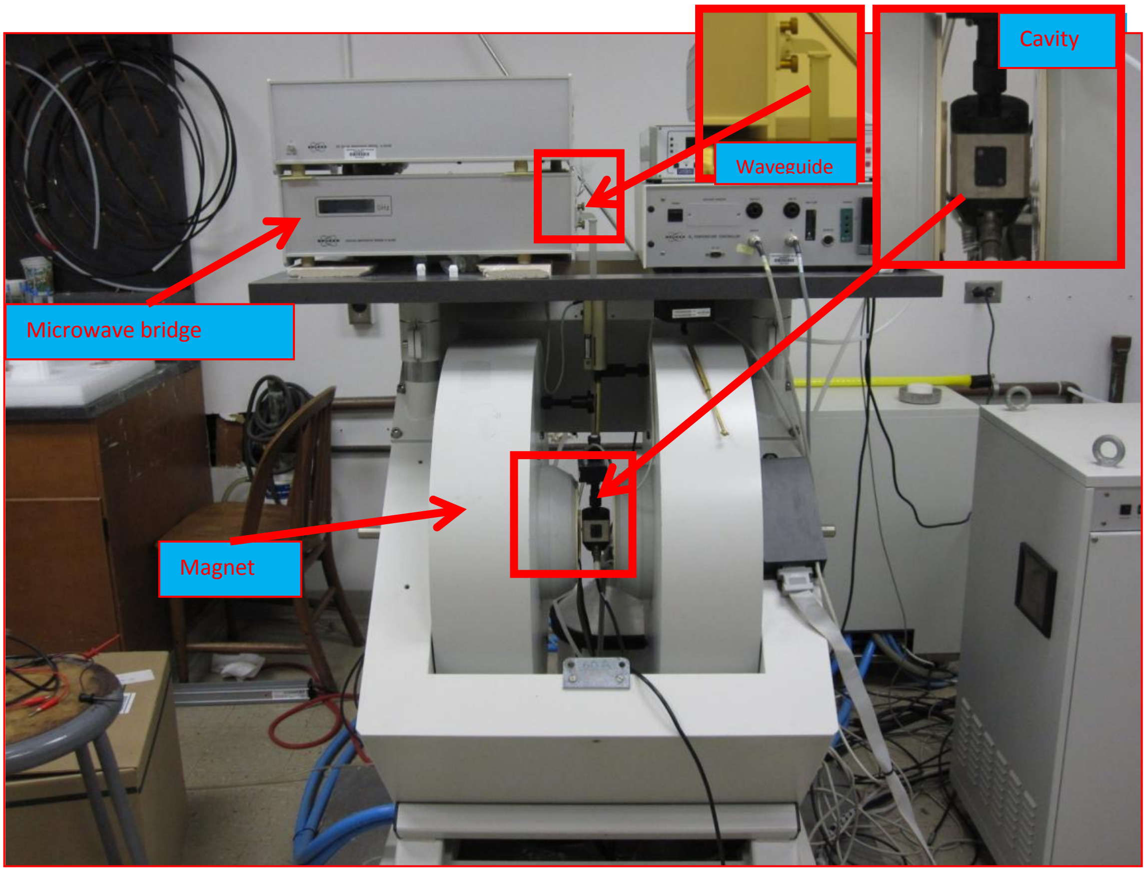

Fig 3.2c: Photograph of EPR spectrometer in AMRI lab (Bruker make)

3.3 Broadband Measurement (Vector Network Analyzer)

A network analyzer consists of a microwave source, a transducer to convert the microwave signal and the response signals produced by the device under test to a set of output signals. The microwave network analyzer measures complex ratio by the technique of frequency translation by sampling. Sampling is a signal processing in which, the input signal is translated to a lower, fixed IF frequency. So all the processing after that is done at the same frequency, the IF. This makes the processing simpler because it is difficult to make amplifier, detector and filters that can be tuned to different frequency. Without using an IF, the filters and detectors would have to be tuned in unison for response obtained from each frequency in broadband (for Network analyzer in our lab frequency sweep is from 50 MHz to 40 GHz).

The IF signals reconstructed from the sampler outputs are both 20-MHz signals, but since frequency conversion is a linear process, these signals have the same relative amplitudes and phases as the microwave reference and test signals. Thus gain and phase information are preserved.

Two port network

Although a network may have any number of ports, network parameters can be explained most easily by considering a network with only two ports, an input port and an output port.

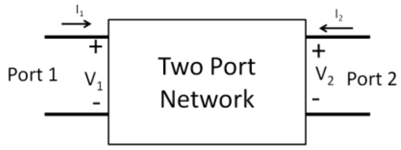

Fig3.2d: A general two port network

Each parameter set is related to a set of four variables associated with the two-port model. Two of these variables represent the excitation of the network (independent variables), and the remaining two represent the response of the network to the excitation (dependent variables). If the network of Fig. 3.2d is excited by voltage sources V_1 and V_2, the network currents I_1 and I_2 will be related by the following equations (assuming the network behaves linearly).

$$I_1 = y_{11}V_1 + y_{12}V_2 \qquad 3.2a$$

$$I_2 = y_{21}V_1 + y_{22}V_2 \qquad 3.2b$$

In the case when port voltages are independent variables and port currents taken as dependent variables, the relating parameters are called short-circuit admittance, or y-parameters. In the absence of additional information, four measurements are required to determine the four parameters y_{11}, y_{21}, y_{12} and y_{22}. Each measurement is made with one port of the network excited by a voltage source while the other port is short circuited. For example, y_{22}, the forward transadmittance, is the ratio of the current at port 2 to the voltage at port 1 with port 2 short circuited is given by,

$$y_{21} = \left.\frac{I_2}{V_1}\right|_{V_2=0\text{(Output short circuited)}} \qquad 3.2c$$

S parameter

S-parameters (or scattering parameters) are now more common in microwave design because they are easier to measure and work with at high frequencies than other kinds of parameters. They are conceptually simple, analytically convenient, and give good insight into a measurement or design problem. S-parameters are usually measured with the device imbedded between a 50 Ω load and source. Measuring S-parameters is obtained by measuring (a) the ratio of the magnitudes and (b) the relative phase angles of response and excitation signals at the ports of a network with the other ports terminated in a specified impedance.

Generalized scattering parameters were first defined by K. Kurokawa. These parameters describe the interrelation ships of a new set of variables (a_i, b_i). The variables a_i and b_i are normalized complex voltage waves incident on and reflected from the i^{th} port of the network. They are defined in terms of the terminal voltage V_i, the terminal current I_i, and an arbitrary reference impedance Z_i, as follows

$$a_i = \frac{V_i + Z_i I_i}{2\sqrt{|\mathrm{Re} Z_i|}} \quad b_i = \frac{V_i + Z_i^* I_i}{2\sqrt{|\mathrm{Re} Z_i|}} \qquad 3.2d$$

The linear equations describing the two port network are:

$$b_1 = S_{11}a_1 + S_{12}a_2 \qquad 3.2e$$

$$b_2 = S_{21}a_1 + S_{22}a_2 \qquad 3.2f$$

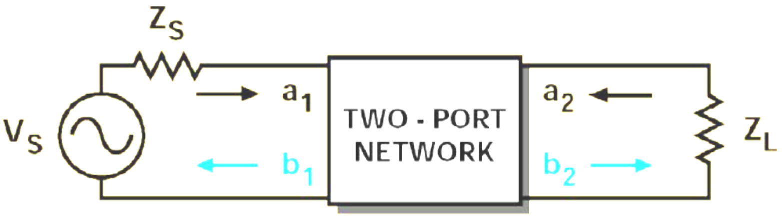

Fig 3.2e: Two-port network showing incident (a1, a2) and reflected (b1, b1) waves used in s-parameter definitions

The physical interpretation of S parameters S_{11}, S_{22}, S_{21}, and S_{12} are as follows:

$S_{11} = \left.\frac{b_1}{a_1}\right|_{a_2=0}$ = Input reflection coefficient with the output port terminated by a matched load

(Z_L=Z_0 sets a_2=0).

$S_{22} = \left.\frac{b_2}{a_2}\right|_{a_1=0}$ =Output reflection coefficient with the input terminated by a matched load

(Zs=Z_0 sets Vs=0).

$S_{21} = \left.\frac{b_2}{a_1}\right|_{a_2=0}$ = Forward transmission (insertion) gain with the output port terminated in a matched load.

$S_{12} = \left.\frac{b_1}{a_2}\right|_{a_1=0}$ = Reverse transmission (insertion) gain with the input port terminated in a matched load.

And the relationship between a_1, a_2, b_1, b_2, and various power waves is:

$|a_1|^2$ =Power incident on the input of the network

=Power available from source impedance Z_0

$|a_2|^2$ =Power incident on the output of the network

= Power reflected from the load

$|b_1|^2$ =Power reflected from the input port of the network

=Power available from Z_0 source minus the power delivered to the input of the Network

$|b_2|^2$ =Power reflected from the output port of the network

= Power incident on the load

3.3.1 Transmission line

Microwave measurements need a way for the transmission of microwave energy with minimum loss. Transmission lines are the one of the methods for microwave propagation with minimum loss. Transmission lines such as coaxial cable and twist pair lines have two separate conductors separated by an insulating dielectric. Microwave propagation in these transmission lines can be analyzed by voltages and current in the circuit. However other group of waveguides like metallic waveguides is described in terms of their electric and magnetic field.

Most transmission lines are designed to operate with only one mode propagating. The transmission line should be smaller in dimension as the wavelength gets smaller to avoid higher order modes

3.3.1.1 Microstripline

Microstrip transmission line is one of the most common transmission line used in microwave circuits (Fig3.3.1.1.b). It can be manufactured by photolithography or chemical etching method

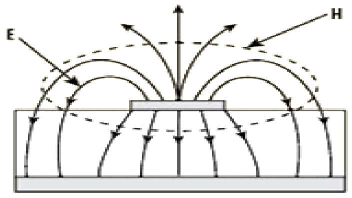

Fig 3.3.1.1a: Electric and magnetic field profile in a microstripline

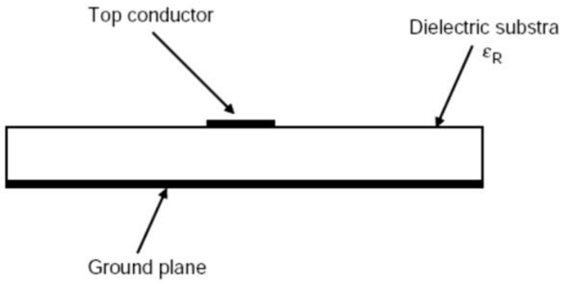

Fig 3.3.1.1b: Cross section of a microstrip transmission line

The velocities of waves are in the range

$$\frac{3 \times 10^8 \mathrm{m/sec}}{\sqrt{\varepsilon_\mathrm{R}}} < v < 3 \times 10^8 \mathrm{m/sec}$$

Where $\varepsilon_\mathrm{R}$is relative permittivity of the substrate. The cut off frequency of microstrip can be found by critical wavelength λc given by

$$\lambda c = 2W$$

where W is the width of the top conductor.

Microstrip has much less dispersion compared to rectangular waveguide; however attenuation in microstrip is much greater. Characteristic impedance can range from 5-150 Ω. One more concern with the microstrip is that it radiates. So, care should be taken and circuit needs to be enclosed to prevent radiation.

3.3.1.2 Coplanar waveguide

These types of waveguides have comparatively small dispersion. The cross section of the coplanar waveguide is shown in the Fig3.3.1.2a and the field distribution is given in the Fig3.3.1.2b and Fig3.3.1.2c. Characteristic impedance ranges from 25-100 Ω depending on the width of the slots and relative permittivity of the substrate. The velocity of coplanar waveguide is given by

$$\mathrm{v} = \frac{3 \times 10^8 \mathrm{m/sec}}{\sqrt{(\varepsilon_\mathrm{R}+1)/2}} \qquad 3.3.1.2a$$

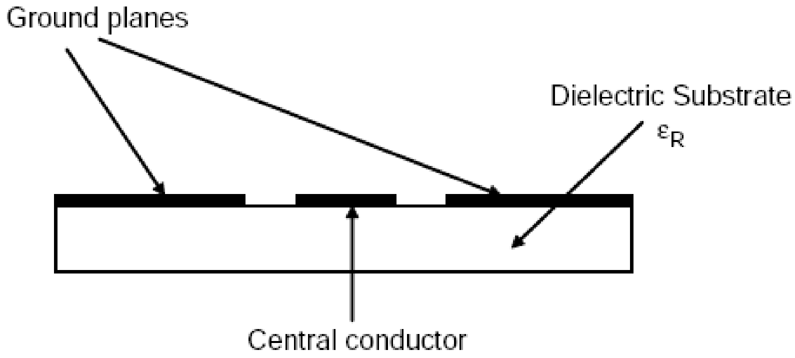

Fig 3.3.1.2a: Cross section of a coplanar waveguide

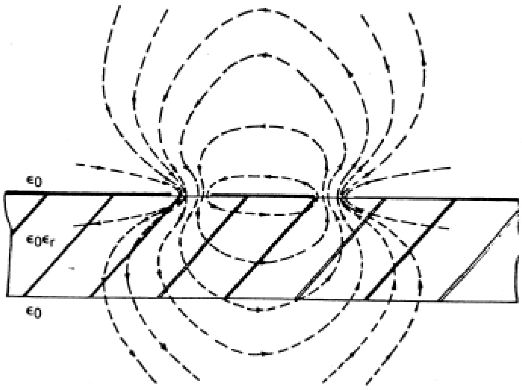

Fig 3.3.1.2b: Computed magnetic field distribution in the cross section

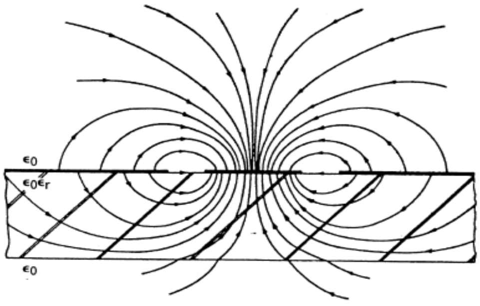

Fig 3.3.1.2c: Computed electric field distribution in the cross section

Chapter 4 Broadband and X-Band FMR of ordered Ni Nanowire

4.1 Introduction

In this chapter we discussed two different works done with Ni Nanowire. First one was development of broadband FMR technique using Vector Network Analyzer (VNA). Measurements were done on nickel Nanowires in two different geometrical configurations viz. microstripline and coplanar waveguide. Nanowires were grown in alumina template provided byJagnyaseni Tripathy working in professor's John Wiley group.

In second part we continued X-Band FMR on complex array of Ni Nanowires arrays of different diameter and interpore distance having different strength of dipolar interaction. Further we have correlated the data obtained from First Order Reversible Curve (FORC). The Nanowires were provided by Dr. Jin Hee working in professor's John Wiley group

4.1.1 Broadband FMR study of Ni nanowire

We used two types of transmission lines for microwave propagation, microstripline and coplanar Waveguide. On comparing the FMR spectra we found coplanar waveguide configuration is less noisy. The resonance field and resonance frequency obtained from X-Band FMR and from VNA are in close agreement to each other.

Measurement using microstripline

The schematic representation is shown in the fig 4.1.1a and the photograph of the set up in our lab is shown in the fig 4.1.1b.

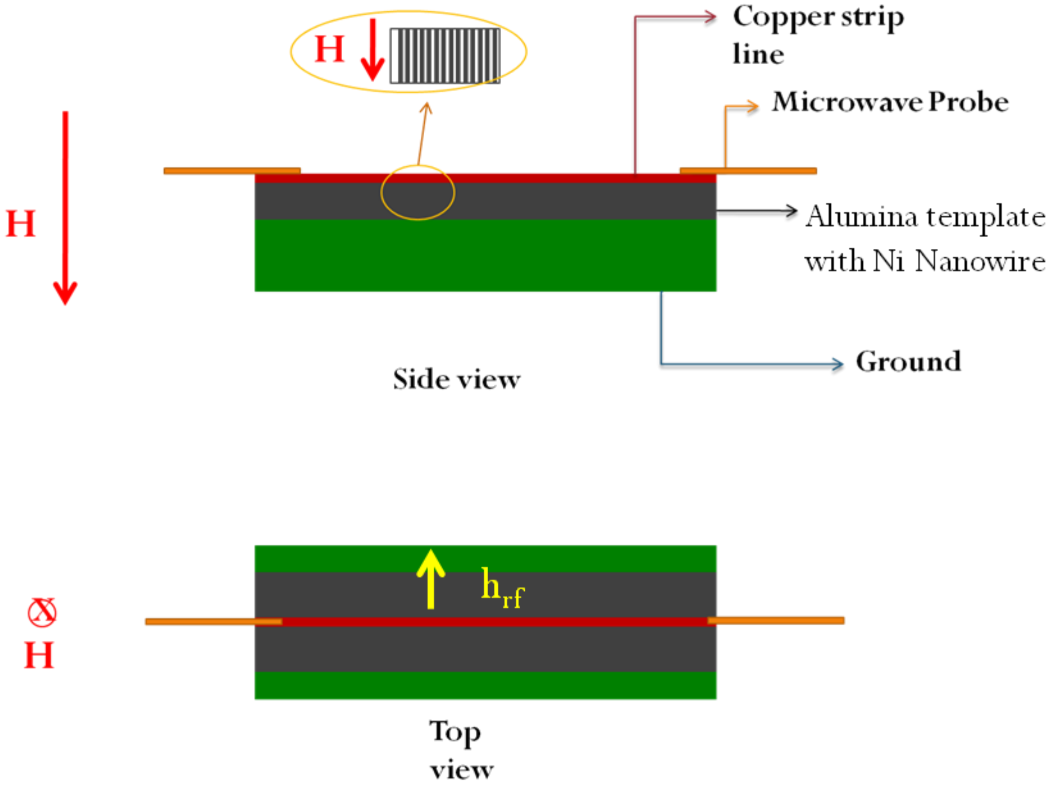

Fig 4.1.1a: Schematic representation of microstripline configuration

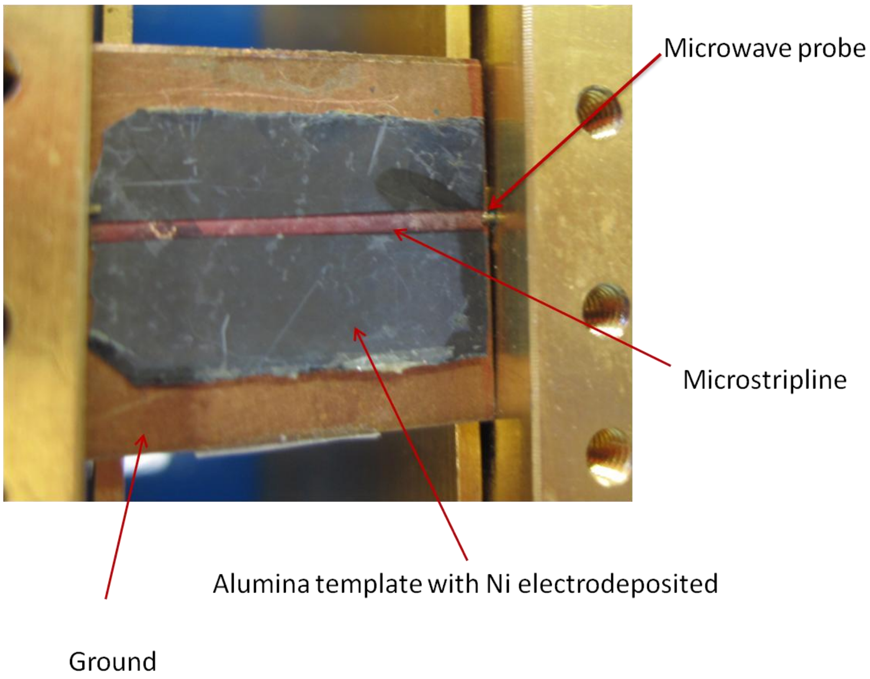

Fig 4.1.1b: Photograph of microstripline setup

The major drawback of this measurement configuration was that the microstrip has to be deposit on the template itself which was very fragile, further it was prone to damage by the probes on multiple measurements. Further, FMR obtained from this method (fig 4.1.1g) was more noisy compared to the one obtained from coplanar waveguide.

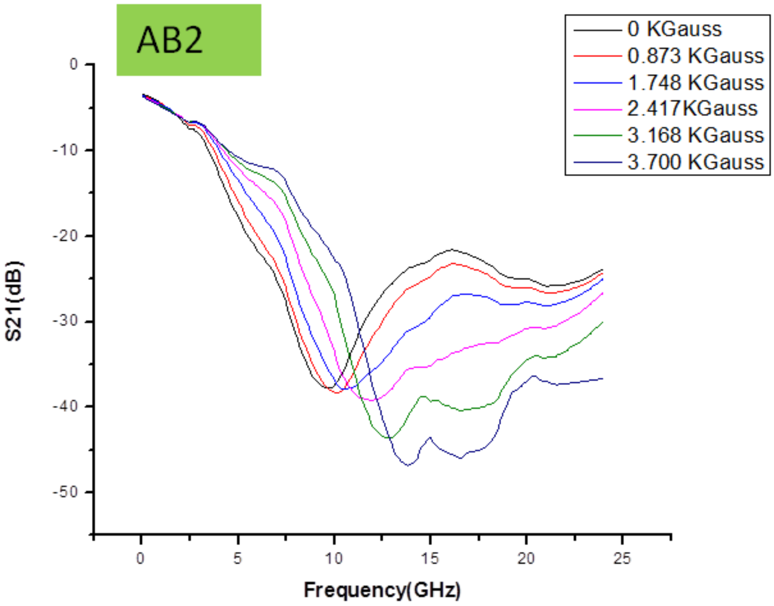

Fig 4.1.1c: FMR obtained from microstripline configuration

Measurement using coplanar waveguide

The schematic representation is shown in the fig 4.1.1d, and the photograph of the set up in our lab is shown in the fig 4.1.1e.

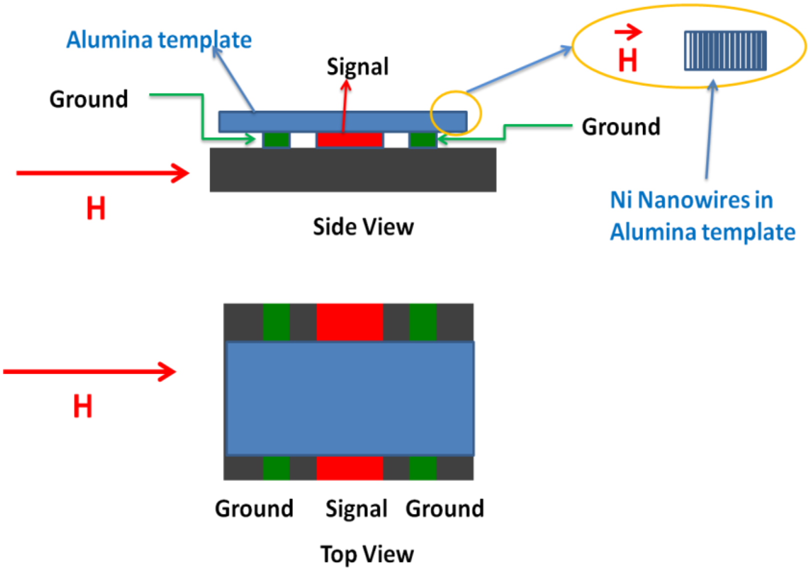

Fig 4.1.1d: Schematic representation of coplanar waveguide configuration

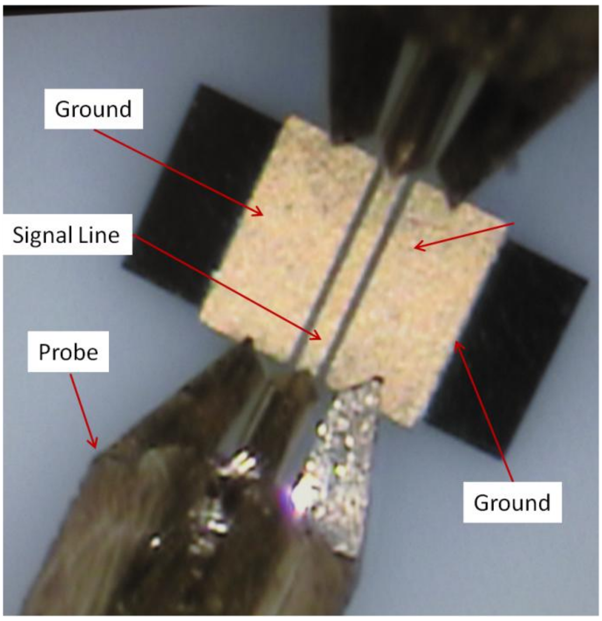

Fig 4.1.1e: Photograph of coplanar waveguide measurement setup

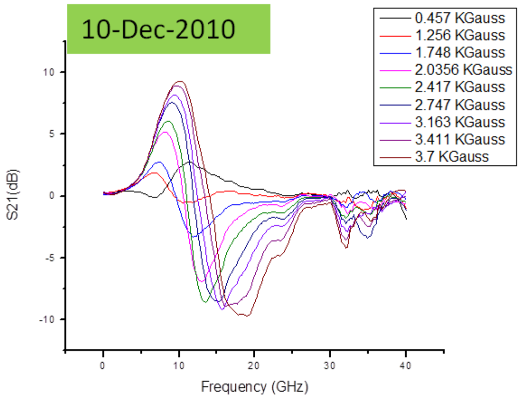

Fig 4.1.1f: FMR obtained from coplanar waveguide configuration

Comparison of results obtained from microstripline and coplanar waveguide

On comparing the FMR using microstripline and coplanar waveguide we can see the results from coplanar waveguide are cleaner fig 4.1.1g.

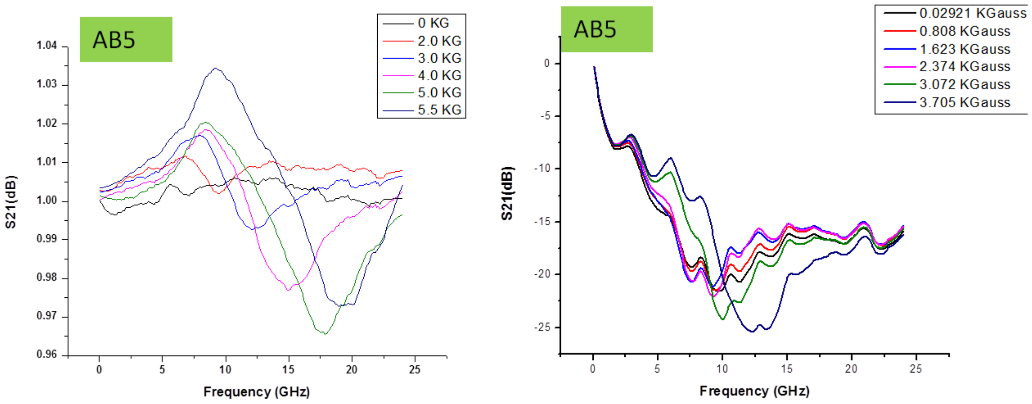

Fig 4.1.1g: FMR obtained from coplanar waveguide (left) and microstripline (right)

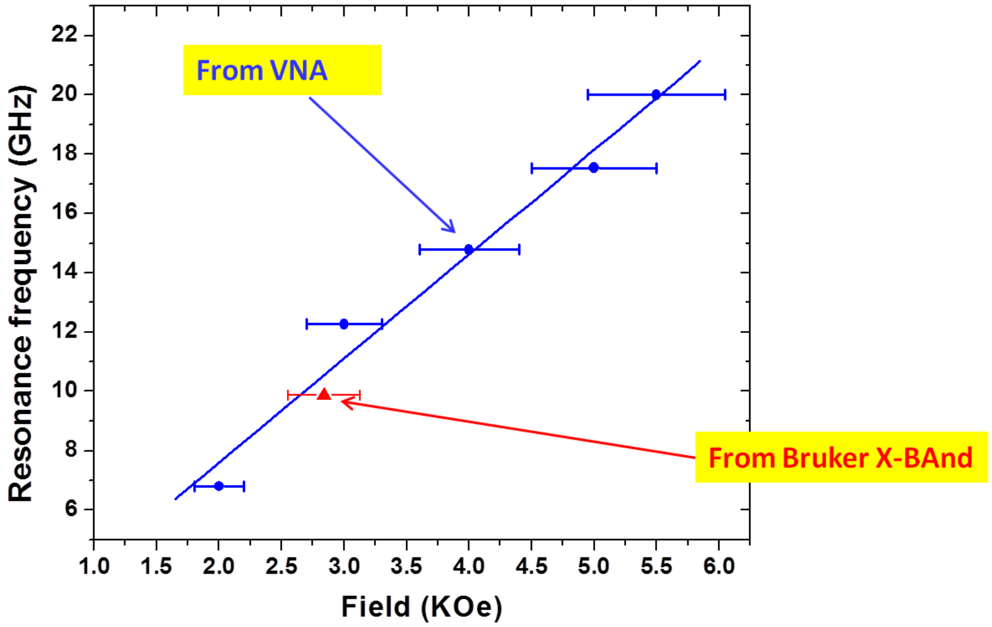

Fig 4.1.1h: Comparing FMR obtained from Broadband measurement and X-Band

4.1.2 X-Band FMR study in complex array of Ni nanowire

An important problem in condensed matter physics involves the microscopic understanding of how dipolar interaction affect the magnetic trends of nanostructure systems.[17-19] A theory that focuses on the excitation of spin-wave modes characterized by intrawire exchange and inter-wire dipolar coupling has been developed. Recently, Brillouin light scattering has confirmed the appearance of quantized spin-wave in these Ni NW arrays[20]. Ebels *et al.* [21] studied ferromagnetic resonance (FMR) of Ni NW of various diameters grown on polycarbonate membranes. The dipolar interactions between the wires can be modeled in a mean-field approach as an effective uniaxial anisotropy field oriented perpendicular to the wire axis and proportional to the membrane porosity. The dipolar interaction field competes with the internal anisotropy field of an isolated single wire (which keeps the magnetization parallel to the wire axis). An increase in the porosity therefore induces a switching of the effective anisotropy easy axis from parallel to perpendicular to the wire axis above a critical porosity of 35-38 % independent of the wire diameter[15]. In principle, FMR would be one of the main techniques to bring insights to this problem since it could probe directly the Ni Nanowires itself and interaction among them. Meanwhile, First Order Reversal Curve (FORC) method, obtained from conventional VSM or AGM magnetometry, gives some idea about quantitative distribution of magnetic interactions and distinguishing reversible and irreversible magnetization switching process.[16, 22, 23].

Ramos *et al.*,[24] reported FMR experiments in hexagonal arrays of weakly interacting Ni Nanowires, where the spectra shows a main line associated with a uniform mode, and the angular variation of this line is characteristic of an easy axis along the wire length. Similar results were reported by Dumitru and co-workers,[25] where the experimental hysteresis loops and FMR spectra were interpreted using a statistical method that is based on the integration of the static and dynamical response in the Preisach plane.

Denardin *et al.*, [26] reported the dependence of the coercivity of the arrays as a function of the length of the Ni Nanowires by FORC, where the FORC diagrams provide detailed information about the field distribution of interactions and coercivities. Whereas, Menard *et al.*,[27] reported the magnetization reversal in arrays of Ni Nanowires with different diameters, at 20 nm, 40 nm and 170 nm, showing that the magnetic response is a combination of coherent and incoherent rotation of magnetization of the Nanowires.

In spite of several systematic works proved the effect of the dipolar interaction taking into account different Nanowire lengths, filling fractions and geometrical arrangements, the correlation between static and dynamic techniques remains unexplored.

With the aim to mapping the dipolar interaction strength in the magnetic response of Nanowires, in this work we reported FMR measurements performed at X-band (~ 9.5 GHz) and at temperatures of T = 4.2 K and room temperature, in three samples of Ni Nanowires with filling fraction values of f = 20 %, 33 % and 47 %.The samples were prepared by the method described in reference [28].

We have studied the static and dynamic effects of the dipolar interaction with different diameters and different interwire distances. This is essential for a correct evaluation of the effect of the interactions in magnetic Nanowire arrays, as it is well known that Nanowire arrays with different diameters are subjected to different strengths of interaction. The X-band (~ 9.5 GHz), Ferromagnetic Resonance (FMR) results and the direct analysis of their parameters allowed us in mapping the contribution of the intrinsic anisotropy field of Ni Nanowires and the effect of dipolar interaction. These results are supported by static First Order Reversal Curve (FORC) analysis. The FMR angular variation of the resonance field, H_R, and linewidth, ΔH_{pp}, followed the expected trends for the case of intrinsic uniaxial anisotropy field of the Ni Nanowires, and proved the thermal dependence with the dipolar interaction. Meanwhile FORC diagram showed the effect of the dipolar interaction, reflected in the HC distribution. Moreover, the FORC diagrams showed the fingerprint of memory effect in the particular case of weak and intermediate interaction.

4.1.2.1 Experimental technique

Three samples of Ni Nanowires were prepared by deposition in anodic aluminum oxide (AAO) membranes, corresponding a filling fraction values of f = 0.20, 0.33 and 0.47 for weak, intermediate and strong strength of the dipolar interaction, respectively as was reported by A.Rotaru etal [28]. The membranes were prepared by either a two or three-step anodization procedure. Ni Nanowires were grown in the pores of AAO templates by electrodeposition. Initially an Ag film was sputtered onto one side of AAO template. Metal Nanowires were then grown over several minutes at room temperature in constant current mode at 0.5 mA on a Princeton Applied Research VMP2 galvanostat with a Platinum wire as counter electrode. A commercially available Ni plating solution (Technics Inc., Nickel sulfamate-RTU) was used. The following samples were prepared: The Mild-Hard (MiHa) sample, where the mean diameter of the Nanowires is 70 nm, the interpore distance is about 250 nm and the length is 15.8 µm. The Hard-Mild (HaMi) Nanowires, with a mean diameter of 110 nm, interwire distance of 250 nm and length of 15.0 µm. The Single Modulated (SM-MiHa) templates are identical to MiHa and HaMi, but here wires are grown such that they cross the mild and hard interface, starting from the mild side, to produce single modulated diameter structures with a full length of 30.8 µm. Fig 4.1.2.1a (top) shows the schematic view of these three samples and Fig 4.1.2.1a (bottom) the Scanning Electron Microscopy (SEM) images of each one. Table 1 summarizes the structural information for MiHa, HaMi and SM-MiHa samples.

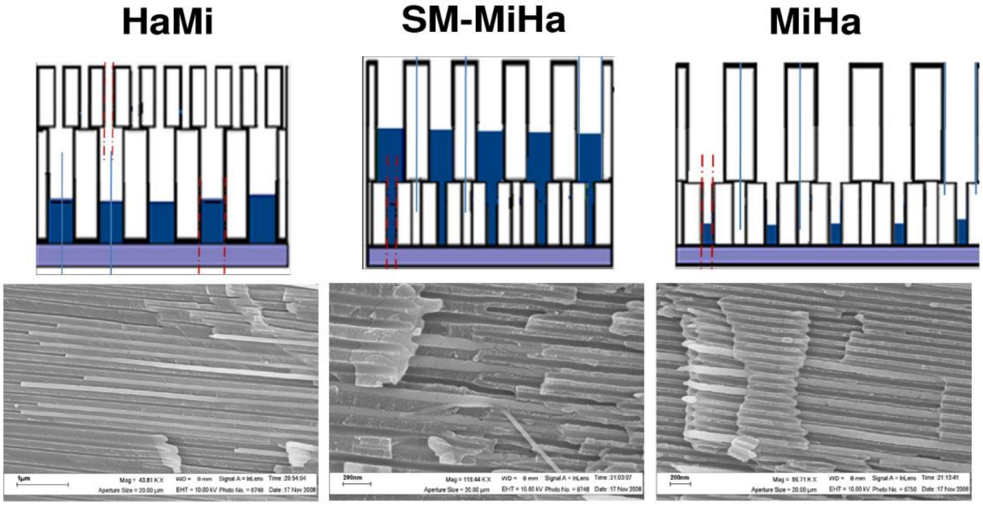

Fig 4.1.2.1a: Schematic view of the three samples of Ni Nanowires supported on AAO template (top). Cross-section SEM images for MiHa, HaMi and SM-MiHa samples (Bottom).

The ferromagnetic resonance (FMR) measurements were performed using a Bruker EMX spectrometer operating at 9.402 GHz (X-band), modulation field frequency at 100 kHz and amplitude of 3 Oe. To improve the signal-to-noise ratio, the microwave power was fixed conveniently at 0.35 mW. In a typical experiment, the magnetic field was driven from 0 Oe to 8 kOe, with a sweeping time of ~ 41 s (195 Oe/s). A commercial gas flow cryostat was used which allowed to achieve temperatures in the range of 4.2 – 300 K. The cavity itself was kept at room temperature and its quality factor was not changed upon cooling. The FMR angular variation was carried out for each sample, with an angle step of 3°, where 0° and 90° degrees were related to the conditions of magnetic field parallel and perpendicular to the Nanowires, respectively. From the single-line absorption-derivative FMR spectra, two characteristic parameters were defined: The resonant field H_0 as the center point of the spectrum, and the peak-to-peak line width ΔH_{pp}. The magnetic measurements (major hysteresis loops (MHL) and FORCs) were done at room temperature on a Princeton AGM-VSM Magnetometer (using the VSM option).

4.1.2.2 Results and discussions

4.1.2.2.1 FORC analysis

Fig 4.1.2.2.1a presents the typical family of FORCs for each sample, and fig 4.1.2.2.1b shows the FORC diagrams of MiHa (15.8 µm), HaMi (15.0 µm) and modulated SM-MiHa (30 µm) composed of two 15.0 µm long sections of diameters 70 nm and 110 nm. From the local interaction field distribution profiles (ρ_u) showed in the right side panel one observes that the strength of dipolar interaction in the single modulated diameter Nanowire array sample is intermediate between interactions in MiHa (weak strength of interaction) and HaMi (strong strength of interaction) samples. Also, the maximum of the profiles for the three samples were symmetric and isotropic, i.e., the maximum is centered near to zero magnetic fields. The local coercive field distribution profiles (ρ_C) shows a more complex distributions, where in the case of MiHa and SM-MiHa, both samples showed a bimodal distribution, whereas HaMi presented a broad single distribution.

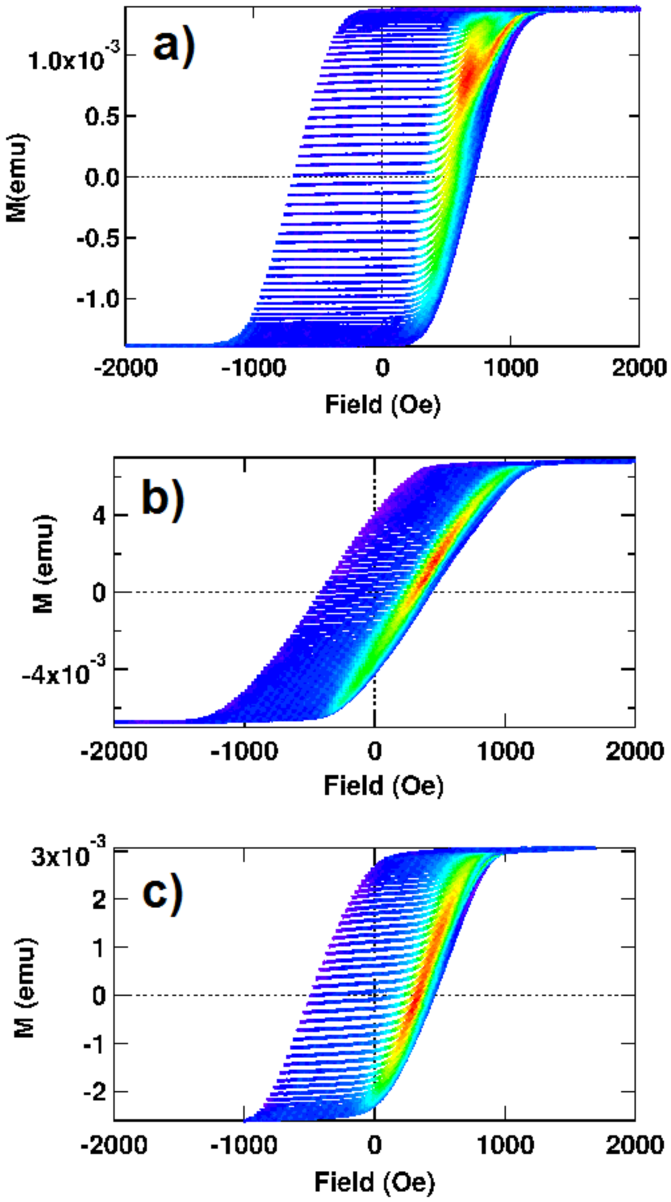

Fig 4.1.2.2.1a: Typical family of FORCs for a) MiHa, b) HaMi and c) SM-MiHa samples, measured at Room-T. The color lines show their contribution to the FORC diagrams (see their correlation with FORC diagrams in 4.1.2.2.1b

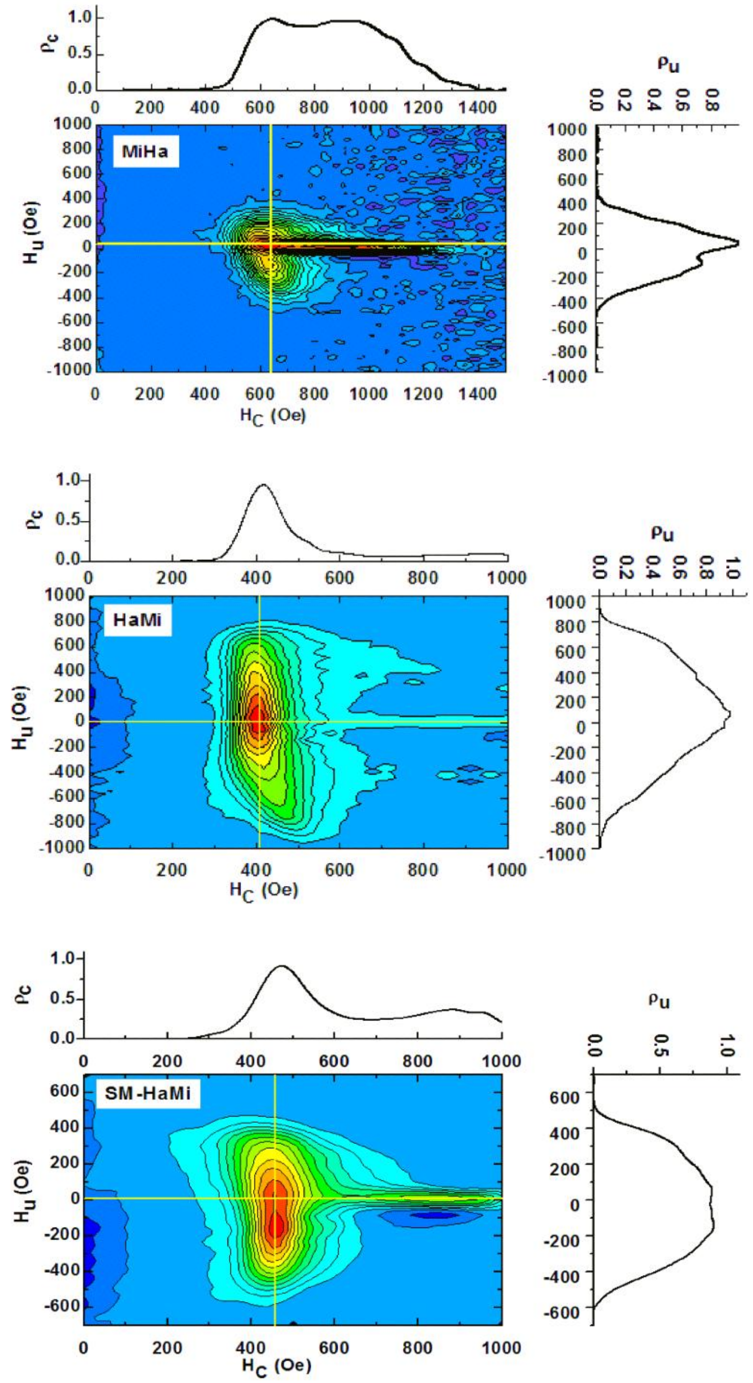

Fig 4.1.2.2.1b: FORC diagrams of MiHa (15.8 µm), HaMi (15.0 µm) and modulated SM-MiHa (30 µm) composed of two 15.0 µm long sections of diameters 70 nm and 110 nm.

By increasing the Nanowire diameter, while the distance between their centers remains constant, the mean interaction field is also increasing, due to the closer proximity of the wires-walls (180 nm (MiHa) *vs* 140 nm (HaMi)). Moreover, the standard deviation of interaction field distribution, σ_u, increases more than two times, while the most probable value and standard deviation of coercive field distribution varies only slightly. This is a clear indication of the increased effect of interwire interaction as only the distance between Nanowires is decreasing. Furthermore, one observes subtle differences in the way the interaction field is decaying on moving away from the $H_u = 0$ line. Thus, in the MiHa sample the dipolar interactions are localized with a quasi-linear decay of the interaction field, while in the HaMi sample the interaction field is broadly distributed with a convex decay. The combination of the two aforementioned effects in the single modulated diameter Nanowire samples results in an intermediate width of the interaction field distribution with a localized convex decay.

By increasing the wire diameter one observes a variation of the coercive field mean value from $H_{C1} = 617$ Oe, for a Nanowire diameter of 70 nm (MiHa sample) down to 400 Oe, for a diameter of 110 nm (HaMi sample). This is consistent with a variation of the coercive field inverse proportional with the diameter previously observed in similar systems [29] and associated with a non-coherent magnetization reversal in the case of magnetic Nanowires with diameter larger than the critical diameter D_{coh} which for Ni is 26 nm [30-32].

Essentially, for these samples the second distribution peak in ρ_c is part of the reversal field memory ridge. Thus, by a careful choice of methods of preparing high quality templates one can obtain complex magnetic Nanowire systems with tunable magnetic properties.

Table 4.1.2.2.1: Structural and Statistical analysis of the FORC distributions

Sample	H_{C1} (Oe)	σ_{c1} (Oe)	H_{C2} (Oe)	σ_{c2} (Oe)	H_u (Oe)	σ_u (Oe)
MiHa-15.8μm	617	77	933	193	-17	182
HaMi-15.0μm	400	72	--	171	27	460
SM-MiHa-(14+16) μm	436	80	766	146	-23	309

4.1.2.2.2 FMR (X-band): Temperature effect and angular variation

Fig 4.1.2.2.2a presents the room-*T*, X-band (9.401 GHz), FMR spectra of MiHa, HaMi and SM-MiHa samples, measured at different angular orientations against magnetic field. The samples are positioned in such way that the angle value of $\varphi = 0°$ and 90° correspond to the magnetic field along and perpendicular to the Ni Nanowires, respectively. Fig 4.1.2.2.2b shows the FMR spectra for the three samples recorded at low-$T = 4.4$ K and at different angular orientations.

The resonance condition for uniaxial ferromagnet is given by the Smith and Beljers equation:[10, 11]

$$\left(\frac{\omega}{\gamma}\right)^2 = \frac{1}{M_r^2}\left(M_r H\cos(\varphi-\varphi_H) - 2\pi M_r^2(\sin^2\varphi - 1)\right)\left(M_r H\cos(\varphi-\varphi_H) + 2\pi M_r^2\cos(2\varphi)\right), \quad (3)$$

with the bounding condition of

$$\sin(\varphi)\cos(\varphi) + \frac{H}{2\pi M_r}\sin(\varphi-\varphi_H) = 0, \quad (4)$$

where $\omega = 2\pi\nu$, ν is the microwave frequency (~ 9.4 GHz), $\gamma = \frac{g\mu_B}{\hbar}$, *g* is the gyromagnetic value, μ_B is the Bohr magneton, $\hbar$ is the planck's constant, M_r is the non-relaxing magnetization of the Ni Nanowire, H is the external magnetic field, φ is the angle between the Ni Nanowire axis and the magnetization (M_r) and φ_H is the relative angle between the Ni Nanowire axis and the external magnetic field. If the effective anisotropy field or demagnetization field is defined as $H_A = 2\pi M_r$, under conditions of $H > H_A$ and $\frac{\omega}{\gamma} > H_A$, the value of the intrinsic anisotropy field can be obtained through the FMR angular variation as $H_\perp - H_\parallel = \frac{3}{2} H_A$ for more details refer to page21 Chapter1.

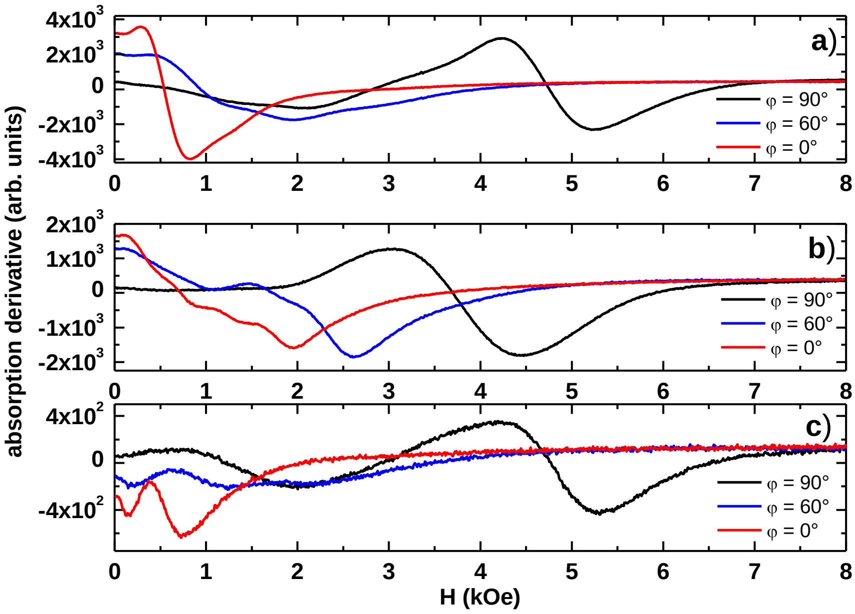

Fig 4.1.2.2.2a: Room-T, X-band, FMR spectra of a) MiHa, b) HaMi and c) SM-MiHa samples, measured at different angular orientations against magnetic field. The sample are positioned in such way that the angle value of θ = 0° and 90° correspond to the magnetic field along and perpendicular to the Ni Nanowires, respectively.

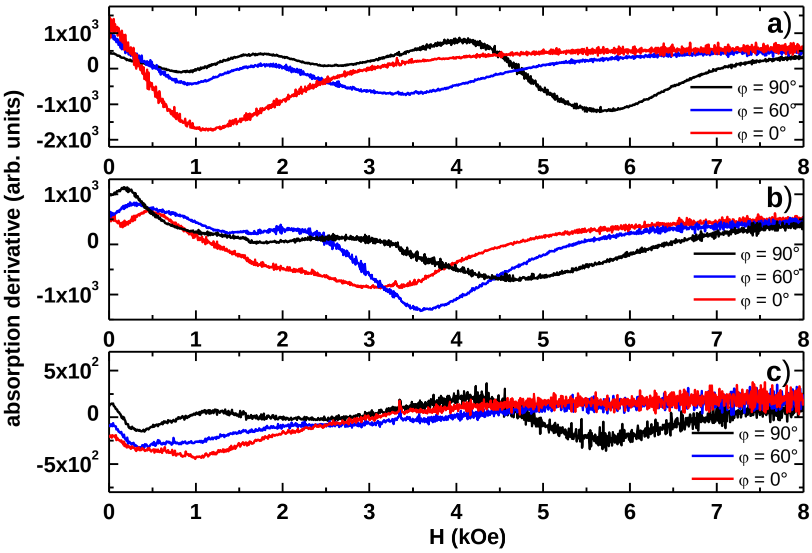

Fig 4.1.2.2.2b: Low-T = 4.4 K, X-band, FMR spectra of a) MiHa, b) HaMi and c) SM-MiHa samples, measured at different angular orientations against magnetic field.

From the FMR line shapes and angular variation of the resonance field (H_R), the following conclusion can be made.

- We identified the uniform mode as the most intense line in the spectra and determined its position performing a fit using a Lorentzian line shape (plus a background) in the region of interest. The additional structure observed may be due to spin-wave excitations [24].
- As the temperature is decreasing, the FMR intensity drops monotonically for the three samples. In particular, a factor ratio of 2.5 (MiHa), 3.0 (HaMi) and 1.5 (SM-MiHa) were obtained between the peak-to-peak intensity measured at room-*T* and 4.2 K. This trend can be related to the broadening of FMR lines at low-*T* due to dipolar interaction among the nanowires.

- Comparing the FMR line-shapes for the three samples at low-*T* (Fig 4.1.2.2.2b), it is noticeable that the modulated sample SM-Mi-Ha shows the fingerprints of both contribution from MiHa and HaMi samples.
- The angular variation of the resonance field (H_R), for MiHa and HaMi samples between $\varphi = 0°$ to 180° shows a single maximum at $\varphi = 90°$ (Fig 4.1.2.2.2c), that it is the expected trend of uniaxial ferromagnet with weakly and intermediate strength of the dipolar interaction, respectively. We remark that the most interacting Ha-Mi sample did not show a switching from easy to hard uniaxial axis, that is expected for filling fraction above the critical value of $f \sim 0.38$.[14, 15].
- In spite of the FORC results at room-*T*, the angular variation for the single modulated SM-MiHa sample is the same measured for the weakly interaction MiHa sample Fig 4.1.2.2.2c:-a)1 However, at low-$T = 4.2$ K the angular variation for SM-MiHa sample is clearly located between the MiHa and HaMi samples Fig 4.1.2.2.2c:-b), indicating that the intrinsic anisotropy strength was successfully tuned between both of them.
- As suggested by Ebels and co-workers, the dipolar interaction field can be modeled in a mean-field approach as an effective uniaxial anisotropy field oriented perpendicular to the wire axis and proportional to the membrane porosity. Therefore, the linewidth of the FMR, ΔH_{pp}, measured at $\varphi = 90°$ orientation, *i.e.*, the magnetic field perpendicular to the Nanowires, is given all the information about the dipolar interaction strength. Whereas, the angular variation of the FMR resonance field, H_R, is given the contribution of the intrinsic anisotropy of the Ni Nanowires. Interestingly from the experimental data at low-*T* and room-*T*, the peak-to-peak linewidth shows the same systematic trend: MiHa sample showed the narrower peak-to-peak linewidth, whereas HaMi gives the broader resonance line. For the

single modulated SM-MiHa sample, the linewidth corresponds to the intermediate case. Fig 4.1.2.2.2d shows the angular variation from φ = 0° to φ = 90° of the line-width (ΔH_{pp}) for the three samples, at room-T and at low-T = 4.2 K. Interestingly, for each sample, the difference between both angular orientations, *i.e.*, $\Delta H_{pp}(\varphi = 90°)$ $\Delta H_{pp}(\varphi = 0°)$, are following exactly the same order of magnitude obtained by FORC analysis. In Table 2 is summarized the FMR parameters obtained from this analysis.

- Using the relationship between the parallel and perpendicular resonance condition (Eq’s 5 and 6), $\mathrm{H}_{\perp} - \mathrm{H}_{\parallel} = \frac{3}{2}\mathrm{H}_{\mathrm{A}}$, the value of the intrinsic anisotropy were obtained for the three samples, in good agreement with the expected values for Ni Nanowires [24].

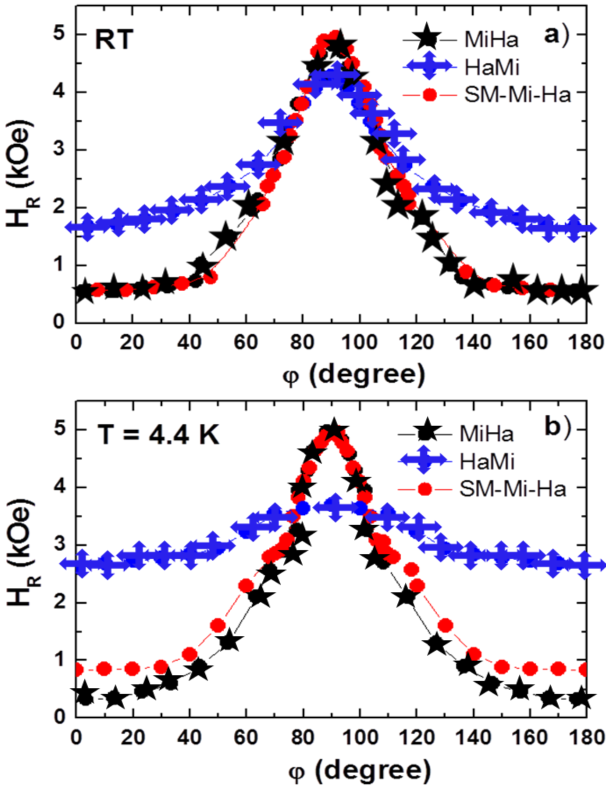

Fig 4.1.2.2.2c: X-band angular variation of the resonance field (H_R) for MiHa, HaMi and SM-MiHa samples measured at a) Room-T and b) Low-T = 4.4 K.

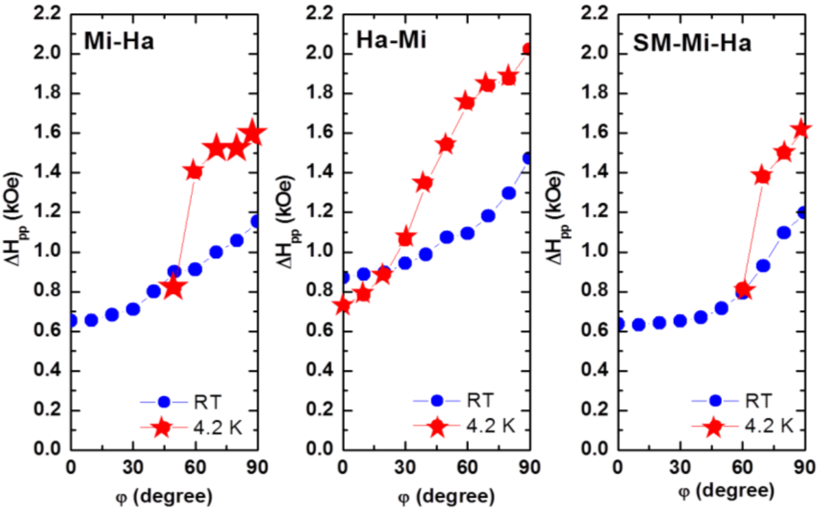

Fig 4.1.2.2.2d: X-band angular variation from $\varphi = 0°$ ($H \parallel$ wires) to $\varphi = 90°$ ($H \perp$ wires) of the line-width (ΔH_{pp}) for the three samples, at room-T and at low-T = 4.2 K.

Table 4.1.2.2.2 FMR results from the angular variation, where H_A is the anisotropy field, $\Delta H_{\varphi=0^\circ}$ are the FMR linewidths when H || and H⊥ to the Ni nanowires

Sample	H_A (Oe) at RT	H_A (Oe) at 4.2 K	$\Delta H_{\varphi=90^\circ}$ (Oe) at RT	$\Delta H_{\varphi=90}$ (Oe) at 4.2 K	$\Delta H_{\varphi=90^\circ}$-$\Delta H_{\varphi=0^\circ}$ at RT
Mi-Ha	**2856**	**3072**	**1160**	**1589**	**505**
Ha-Mi	**1732**	**756**	**1473**	**2027**	**614**
SM-Mi-Ha	**2856**	**2733**	**1200**	**1624**	**579**

4.1.2.3 Conclusions

The effect of dipolar interactions was studied by considering samples with different diameters and different interwire distances as provided by a controlled obstruction of the pores of the AAO templates. This is essential for a correct evaluation of interactions in magnetic Nanowire arrays, as it is well known that Nanowire arrays with different diameters are subject to different strengths of interaction. In fact, the FMR technique showed that from the shape spectra, angular variation of the resonance field and the peak-to-peak linewidth was possible to get direct information about the intrinsic anisotropy and the strength of the dipolar interaction, that it is also supported by FORC analysis. By the FORC technique and through quantitative analysis of their profiles of local interaction and coercive field distributions, a detailed description of the magnetic interactions and magnetization reversal were obtained. Therefore, FORC and FMR, as independent techniques, proved to be a powerful tool to understand the microscopic static and dynamic trends of nanostructure systems.

Chapter5 Ferromagnetic resonance of exchange biased multilayer system (IrMn/NiFe)

5.1 Introduction

Thin films ferromagnetic multilayer systems, core-shell nanoparticles and related systems where at least one antiferromagnetic or metallic-nonmagnetic layer is intercalated between ferromagnetic layers, are an important class of exchange-coupled magnetic nanostructured materials [33-35]

Due to structure imperfections, such as interface roughness, interdiffusion, grain boundary and reduced coordination number at the interface, these structure imperfections further frustrate the exchange-coupled ferromagnetic/antiferromagnetic layers, and new phenomena arise in these systems which makes them ideal candidates for important technological applications in spin-valve-based sensors in hard disk industry [36-38] and microwave devices in the gigahertz range.[39-41] For the above mentioned applications as well as for fundamental studies of magnetic interactions and magnetization reversal in model systems, the most useful configuration is a periodic array of thin ferromagnetic layers where the thickness of the components can be controlled.

Regarding the thickness effect of the antiferromagnetic layer, Chun-Yeol You et al.[42] investigated the dependence of magnetic anisotropies of the exchange-biased NiFe/FeMn/CoFe, where it was observed that uniaxial and unidirectional anisotropies coexists but not collinear to each other, which the angle of misalignment is maximized at very thinner antiferromagnetic layer (~ 5 nm), and converges to zero with further increasing the antiferromagnetic layer thickness.

Nguyen N. Phuoc et al.,[43] performed a detailed characterization of the magnetic and microwave properties of Permalloy–FeMn multilayers grown onto Si(100) and Kapton substrates oriented for frequency range applications between 1- 4 GHz, where a multiple-stage magnetization reversal and consequently a plural ferromagnetic absorption have been observed, which is possibly interpreted in terms of the different exchange interfacial energy acting on each layers.

Shang-Fan. Lee et al.,[44] studied the magnetization dynamic of the exchange bias bilayers system IrMn/NiFe for different thickness of the antiferromagnetic layer, in the frequency range of 1-12 GHz, where a complex correlation between the static and dynamic response were evidenced due to the dynamic anisotropy fields into the damping coefficient.

In this chapter, we describe the dependence of both, magnetic hysteresis and ferromagnetic resonance response, on the magnitude of the exchange bias in multilayer NiFe/IrMn films. In order to vary the exchange bias effect, the thickness of the antiferromagnetic layers was kept constant but the ferromagnetic layer thickness was varied.

5.2 Experimental

5.2.1 Sample detail

The samples were provided by Dr. Carlos Garcia from MIT. Rectangular pieces of 3x12 mm silicon wafer thermally oxidized with 50 nm SiO_2 were used as a substrate. Multilayer films, with a fixed total thickness, of composition [FeNi (t nm)/IrMn (20 nm)] x n(t) were deposited at room temperature using *dc* triode sputtering (t = 20 nm, 60 nm, 80 nm; n = 10, 5, 4), where NiFe represents Ni (80 at.%) Fe (20 at.%).]

Table 5.2.1a: Structural information of the three samples deposited at room temperature using dc triode sputtering.

Sample #	Py t(nm)	IrMn t (nm)	Repetition number	Total thickness (nm)
S2	20	20	10	400
S4	60	20	5	400
S5	80	20	4	400

5.2.2 Major hysteresis loops

Figure 5.2.2a shows the typical magnetization loops for sample S2 at different orientations of the applied magnetic field, *H*, at room-*T*. Due to the intrinsic fabrication process of these samples, the three samples studied in this work showed strong structural-induced anisotropy in plane, in particular, with unidirectional exchange bias field at room-*T*. This fact turns them in striking systems, which means that the exchange bias field is permanently pinned along the long axis of the strips, in one specific orientation (for sample geometry details, see support information). When the magnetic field is applied in-plane, anti parallel to the easy anisotropy axis (labeled as 0° degree orientation), the magnetization loops is shifted toward the positive field axis (Fig. 5.2.2a:-a). Whereas, when the magnetic field is applied in-plane, parallel to the easy anisotropy axis (labeled as 180° degree orientation), the loop is shifted toward the negative field values (Fig.5.2.2a:-b). For the three samples, the ratio between the exchange bias field and coercive field values corresponds to 13, 6.5 and 3.5, respectively. Moreover, looking the general shape of both magnetization loops at orientation values of 0° and 180°, after the initial saturation state and before full inversion of the magnetization, it is noticed a one-step drop of magnetization in a factor $M / M_S \sim 0.85$. This can be related with microstructural defects/roughness of the permalloy layers in the sample, which gives a relative loss of their magnetization, their demagnetization factor, and the loss of their magnetocrystalline qualities.[22, 45, 46] It is worth mentioning that sample S2, S4 and S5 are composed by 10, 5 and 4 layers of Py, respectively (structural information in Table 5.2.1a). The quantification of the intrinsic magnetic properties and inhomogeneities, namely interaction (H_b) and coercive (H_C) field distributions, will be discussed later by the FORC analysis method. In spite of the details mentioned above and the complexity of these multilayer structure, the main results of this preliminary magnetic characterization of the sample S2, S4 and S5, suggest an excellent quality of multilayer films.

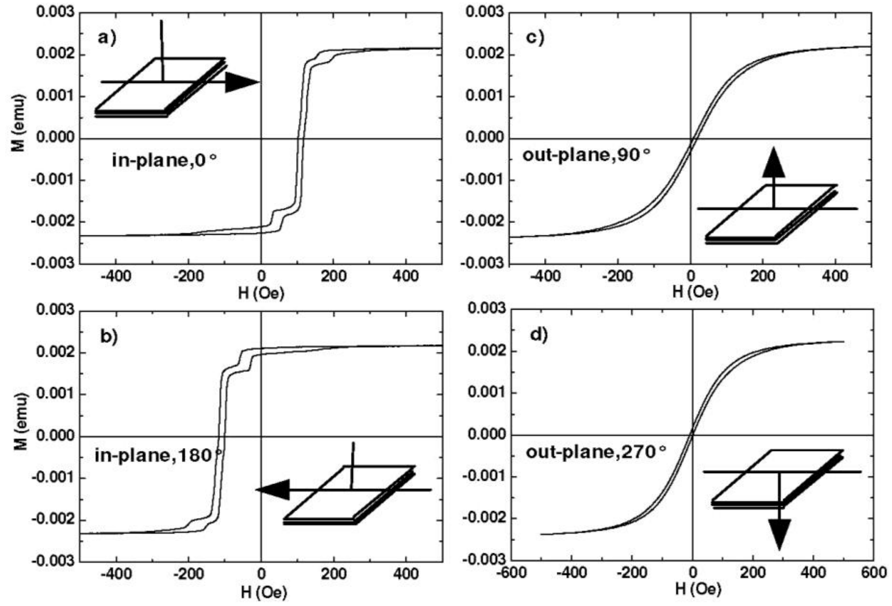

Figure 5.2.2a: The typical magnetization loops for sample S2 at different orientations of the applied magnetic field, H, at room-T.

5.2.3 First Order Reversal Curve (FORC)

The FORC measurement begins with a positive saturation of the samples followed by a ramping down of the applied field to a reversal field H_R. Then the field is increased again up to saturation and magnetization is measured at different values of the applied field H (field step ~ 0.95 Oe). Thus, for different values of the reversal field H_R a family of FORCs is obtained with $M(H;H_R)$ representing the magnetization obtained in the applied field H after a field reversal at H_R. The FORC distributions were obtained by computing the mixed second order derivative of magnetization $M(H;H_R)$:

$$\rho(H, H_R) = -\frac{1}{2}\frac{\partial^2 M}{\partial H_R \partial H}, \qquad (1)$$

using a numerical interpolation algorithm. Specifically, the FORC distributions and diagrams (the contour plots of the FORC distributions) were produced using FORCinel, an algorithm using locally weighted regression smoothing.[47] Usually a new set of coordinates ($H_C;H_u$) are defined with H_C

H_C= $(H-H_R)/2$ and H_u = $(H+H_R)/2$, which rotates the FORC distribution by 45^0. The FORC diagrams as 2D contour plot in coordinate ($H_C;H_u$) for the samples S2, S4 and S5 are shown in the left side of Fig.5.2.3a, respectively. Figure 5.2.3a (right) shows the 200 M $(Hz; H_R)$ FORCs colored waves for each sample, which the color distributions are indicating their contributions to the 2D plot, respectively. In order to quantitatively compare different FORC diagrams obtained for different samples, a statistical analysis was carried out of the profiles of both interaction and coercive field distributions. Hence, the distribution parameters as mean field values of coercive, $<H_C>$, and interaction fields, $<H_u>$, and their corresponding standard deviations, σ_{Hc}, σ_{Hu} were obtained using a single Gaussian distribution function.[48] Also, this was possible to do due to their narrow field distributions. The parameters for all samples considered in this study are given in Table 5.2.4a. In good agreement with the major hysteresis loops, the mean value of the H_u decrease as the Py thickness increase (in this work, the interaction field H_u is equal to the exchange bias field), and their σ_{Hu} distribution is shrinking. In spite of the narrow distributions for all the samples, the sample S2 showed two secondary distributions centered at 67 Oe and 50 Oe, that it could be indicating inhomogeneities in the Py layers in this sample. Meanwhile, the mean value of the coercive field increase as the Py layer thickness increase, with the narrowing of their σ_{Hc}. These results quantitatively prove that i) the exchange bias field induce more homogeneity in the switching field distribution (*i.e.*, proportional to the broadening of the coercive field distribution, σ_{Hc}), where a constant factor ratio of $\sigma_{Hc} / \langle H_u \rangle \sim 7$ % is found for each sample; ii) as the thickness of the Py layer decrease, the magnetic pinning centers and crystalline defects increase, which gives the broadening of both distributions in a factor of $\sigma_{Hu} / \langle H_u \rangle \sim 8$ % (for the three samples) and $\sigma_{Hc} / \langle H_C \rangle = 6.3$, 1.3 and 0.4 for sample S2, S4 and S5, respectively. The values are summarized in Table 5.2.4a.

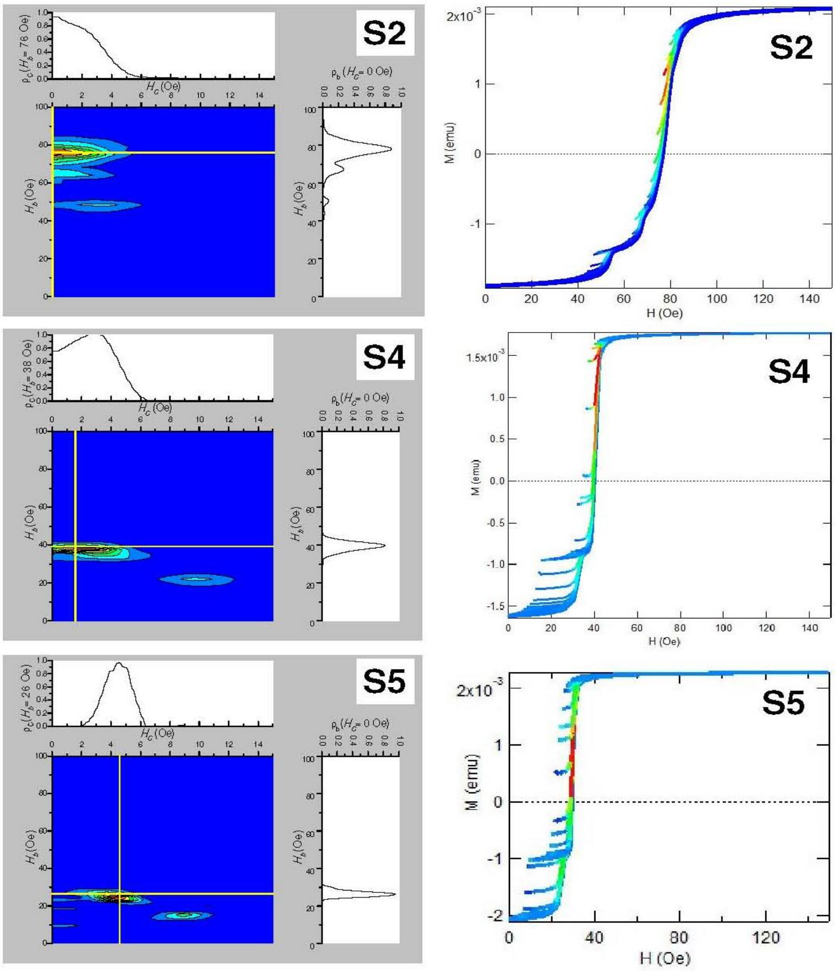

Figure 5.2.3a: The FORC diagrams as 2D contour plot in coordinate (HC;Hu) for the samples S2, S4 and S5 are shown (left). Figure in the right side shows the 200 M(H;HR) FORCs colored waves for each sample, which the color distributions are indicating their contributions to the 2D contour plot, respectively.

5.2.4 FMR X-Band measurement

Ferromagnetic resonance (FMR) and the study of the FMR, angular variation, of ferromagnetic thin films at room-*T* may provide information about internal and demagnetization field effects, magnetocrystalline symmetry, inhomogeneities, skin-depth effect, etc. The FMR spectra of multilayer samples allow not only learning about the whole sample as itself, but also to resolve and study the local contribution of each individual ferromagnetic layer and the interaction between the multiple ferromagnetic layers. The resonance condition for a single “ideal” Py film layer (*i.e.*, without exchange bias field, interlayer interaction and any preferential in-plane orientation for the magnetization), can be given by the Smith and Beljers equation[11]:

$$\left(\frac{\omega}{\gamma}\right)^2 = \frac{1}{M_r^2}\left(M_r H\cos(\varphi-\varphi_H) - 4\pi M_r^2\sin^2\varphi\right)\left(M_r H\cos(\varphi-\varphi_H) + 4\pi M_r^2\cos(2\varphi)\right), \quad (2)$$

With the condition

$$\sin(\varphi)\cos(\varphi) + \frac{H}{4\pi M_r}\sin(\varphi-\varphi_H) = 0, \quad (3)$$

Where $\omega = 2\pi\nu$, ν is the microwave frequency (9.87 GHz), ratio, $\gamma = g\mu_B/\hbar$, g is the gyromagnetic ratio, $\boldsymbol{\mu}_B$ is the Bohr magneton, $\hbar$ is the planck’s constant, M_r is the non-relaxing magnetization of the Py layer, H is the external magnetic field, φ is the angle between the magnetization (M_r) and film plane, and φ_H is the relative angle between the external magnetic field and the film plane. If the effective demagnetization field is defined as $H_A = 4\pi M_r$, under conditions of $H > H_A$, the following relationships can be obtained for both parallel and perpendicular resonance fields:

$$H_\parallel = \frac{\omega}{\gamma} - \frac{H_A}{2}, \quad (4)$$

and

$$H_\perp = \frac{\omega}{\gamma} + H_A, \quad (5)$$

Therefore, using Eq's (4) and (5), the value of the intrinsic anisotropy field (or demagnetizing field) can be obtained through the FMR angular variation as $H_{\perp} - H_{\parallel} = \frac{3}{2} H_A$

Angular variation out-of-plane

Figure 5.2.4a shows the FMR, X-band (9.87 GHz), with out of plane and in-plane, for the three samples at room-*T.* It is worth mentioning that, in the case of FMR in-plane, the magnetic field is applied antiparallel to the easy anisotropy axis (see orientation scheme for position of 0° degree, Fig. 5.2.4b. For sample S2, aside from the narrow lines, several additional absorptions can be observed in the multilayer system`s spectrum. When *H* is applied "out-plane", at least three lines can be distinguished (figure 5.2.4a:--S2) at fields around 12–13 kOe. When *H* is applied "**in-plane**", two resonances are observed at H ~ 1.5 kOe. The line with the largest field variation between the two orientations originates in the first Py layer which was grown directly on the substrate and is certainly continuous and uniform than the subsequent 9 layers, each one with thickness of 20 nm. The next Py layers inherit the roughness of the underlying Py/IrMn layers and could then have a reduced magnetization. In the case of sample S4, a different situation is observed. When *H* is applied "**out-plane**", a single broad resonance is clearly resolved at field up to ~ 9.5 kOe (figure 5.2.4a:-S4). When *H* is applied "**in-plane**", only one resonance is resolved, however, the peak-to-peak aspect ratio and the line broadening suggest a possible convolution of multiple resonances. The field variation between the two FMR resonance orientations leads a considerable lower demagnetization field. In spite of that, the observation of mainly a single broad resonance for both orientations, suggest a better homogeneity between the 5 Py layers, each one with thickness of 60 nm. For sample S5, several additional absorptions can be detected in the multilayer system. When *H* is applied “**out-plane**”, at least three lines can be distinguished (figure 5.2.4a:-S5) at fields around 10–12 kOe. When *H* is applied “**in-plane**”, two resonances are a little resolved for H ~ 1.5 kOe. As it was mentioned for sample S2, similar conclusions can be given in this case, where the line with the largest field variation between the two orientations originates in the first Py layer, which was grown directly on the substrate and is certainly continuous and flatter than the subsequent 3 layers, each one with thickness of 80 nm. For the three samples, using the largest field variation between the two FMR orientations, the values of the effective demagnetization field, H_A, are given in Table 5.2.4a.

Table 5.2.4a: Parameters obtained through FORC analysis (VSM), FMR X-band (9.8 GHz) and VNA broadband (1 GHz-30 GHz).

SAMPLE	VSM-FORC analysis				FMR X-band OUT-plane	FMR X-band IN-plane	VNA-broadband
	$\langle H_u \rangle$ Oe	σ_u Oe	H_C Oe	σ_C Oe	H_A Oe	H_u^{FMR} Oe	$\Delta\omega/\gamma$ Oe
S2	78	6.3	0.7	4.4	7529	75(11)	120
S4	39	3.4	2.8	3.0	5437	45(10)	50
S5	26	2.7	4.5	1.8	6926	25(10)	15

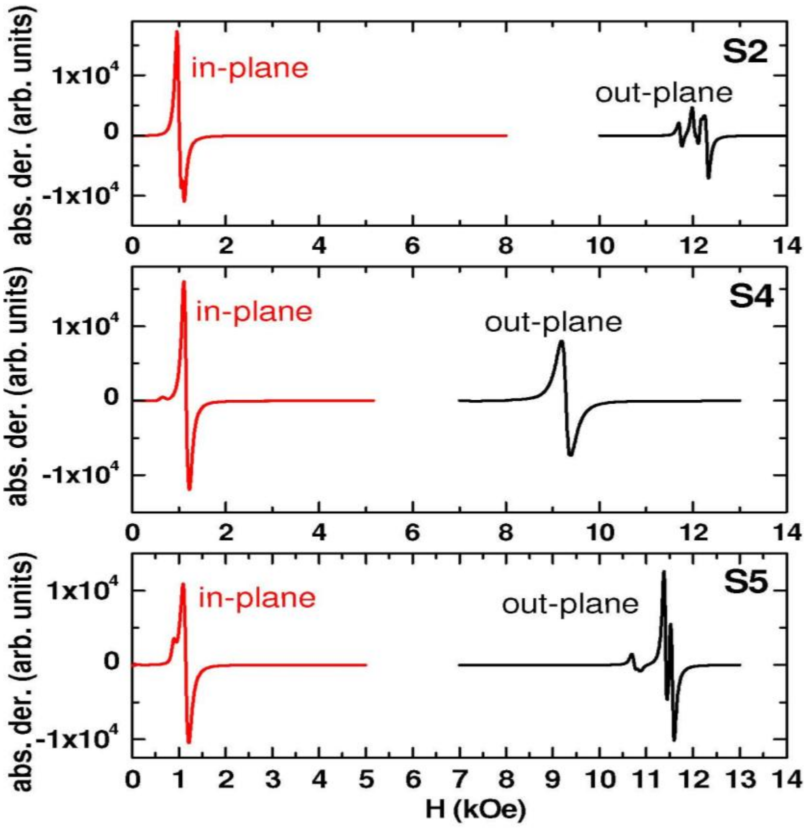

Figure 5.2.4a: FMR, X-band (9.87 GHz), in the conditions of out-plane and in-plane, for the three samples at room-T

Angular variation in-plane

Figure 5.2.4b shows the FMR angular variation, X-band (9.87 GHz), in-plane for the three samples, at room-*T*. At 0° orientation (Fig.5.2.4b:- right), a single FMR line is observed close to H ~ 1150 Oe, with a peak-to-peak linewidth of ΔH_{pp} ~ 110 Oe. As the angular variation increase from 0^{o} to 180°, the single line at 0° splits in two resonances, each one with different angular dependence (Fig.5.2.4b:- right). This means, the three samples showed a 360° “low symmetry condition” in-plane, in good agreement with dc-magnetization measurements. Considering the field variation between the two main FMR orientations at 0° and 180°, the values of the internal exchange bias-field, H_u^{FMR}, were determined for each sample. These values are relatively larger than the mean values obtained by FORC analysis (Table 5.2.4a). Moreover, comparing the intensity ratio between both resonances, the case of sample S5's spectra is basically controlled by only one resonance. Sample S4 showed a little more contribution of the second resonance, whereas in the case of sample S2, the second resonance is better defined and has a greater intensity. Therefore, as it was confirmed in the FMR in plane results, this fact can be explained due to the lower magnetization of the multiple Py layers, given a weak effective exchange-bias field, and the broadening of their distributions for sample S2, S4 and S5. This fact is supported by the FORC analysis discussed above, and the values are summarized in Table 5.2.4a.

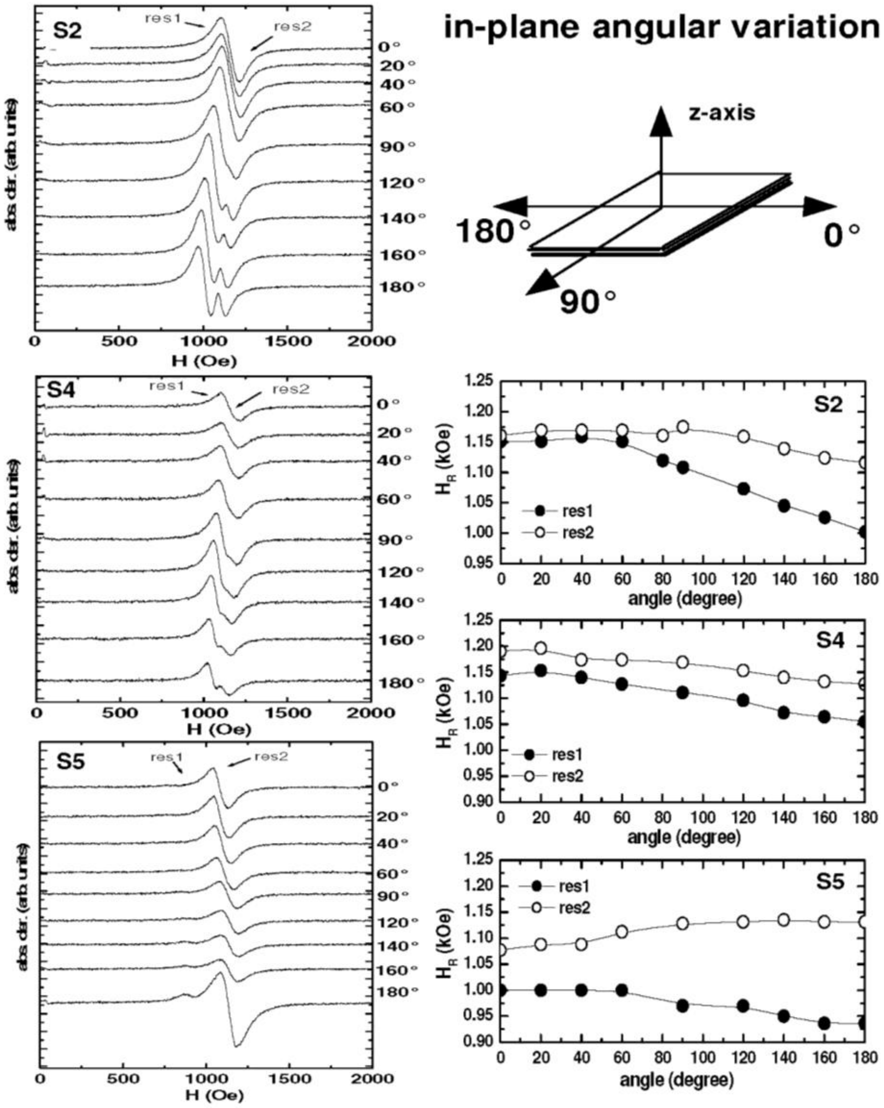

Figure 5.2.4b: FMR angular variation, X-band (9.87 GHz), in-plane for the three samples, at room-T. Spectra for each sample at different angular orientations (Left). Schematic diagram of the sample, 0 degree is defined along the strip direction (right-top). Angular variation of the two resonance fields for each sample (right, bottom).

5.2.5 Broadband measurement

Broadband FMR experiments were carried out in a Vector Network Analyzer (VNA) using a coplanar waveguide on a quartz substrate. Hence, the multilayer samples are positioned on the top the coplanar waveguide. The experimental setup has been optimized to enable frequency sweeps between 1 GHz up to 30 GHz, at bias magnetic field values varying between 0 to 5.5 KOe. The magnetic field is applied parallel to the transmission line (using a Lakeshore probe station). The microwave signal propagation along the transmission line produces a microwave pumping field which is almost perpendicular to the waveguide *i.e.*, perpendicular to the film. In this condition, the microwave pumping field and the bias magnetic field are kept perpendicular to each other such that the perpendicular FMR pumping configuration is always conserved. At resonance frequency there is increased absorption of power from the incident microwave signal and the corresponding minimum in the transmitted power is recorded by VNA.

To get a whole picture of the high frequency FMR response of these samples, broadband FMR experiments were conducted at room-*T*, using a Vector Network Analyzer (VNA), in the setup configuration of coplanar waveguide and magnetic field in-plane. The samples were positioned in such a way that the measurements were conducted with magnetic field parallel and antiparallel with the easy magnetization axis (frequency range from 1 GHz up to 30 GHz). Figure 5 (left) shows the transmission parameter S_{21}, obtained for each sample at 0° and 180° orientations, with a persistent magnetic field at H = 1 kOe, 2.5 kOe and 3.5 kOe. The spectra showed a single broad absorption FMR line, and the difference between both line orientations was clearly seen in the case of sample S2 (Fig. 5.2.5a). The field dependence of each FMR line was measured between 1 kOe up to 5.5 kOe, in which case a linear response was obtained for samples S2, S4 and S5, in both orientations (0° and 180°). Figure 5d) shows the typical field dependence of the FMR line`s spectra for sample S2, in both in-plane orientations. Similar linear response were obtained for sample S4 (Fig.5.2 5b) and S5 (Fig. 5.2.5 c, e) shows the field dependence of the field-gap between both orientations, defined as,

$$\frac{\Delta\omega}{\gamma} = \frac{h}{g\mu_B}\left(\nu_{180} - \nu_0\right), \qquad (6)$$

which shows a mean value, of 250 Oe, 100 Oe and 20 Oe for the samples S2, S4 and S5, respectively. Interestingly, sample S5 that corresponds to the case of thicker Py layer of 80 nm, with 4 layers, showed a little difference between both orientations, giving a small gap with value of 15 Oe. Sample S4 corresponds to the intermediate value of field-gap (50 Oe), and this value is close to the value of the exchange bias field obtained by FMR (at X-band), and the VSM measurements (*i.e.*, the static and dynamics measurements are showing same results). The sample S2 showed a maximum value of the field gap (120 Oe), that it is at least a factor two, greater, than the value obtained from FORC and FMR (X-band) analysis. Figure 5 f) shows a more complete scope of the high frequency FMR response of these samples, with the combination of both results: FMR at X-band (9.8 GHz) in-plane and out-plane, and FMR broadband (in-plane, 1 GHz-30 GHz), and the computer simulated curves (solutions of Eq. 2, and Eq.`s 4 and 5 valid for $H > H_A$) in both orientations for ideal Py film (M_S = 800 Oe).

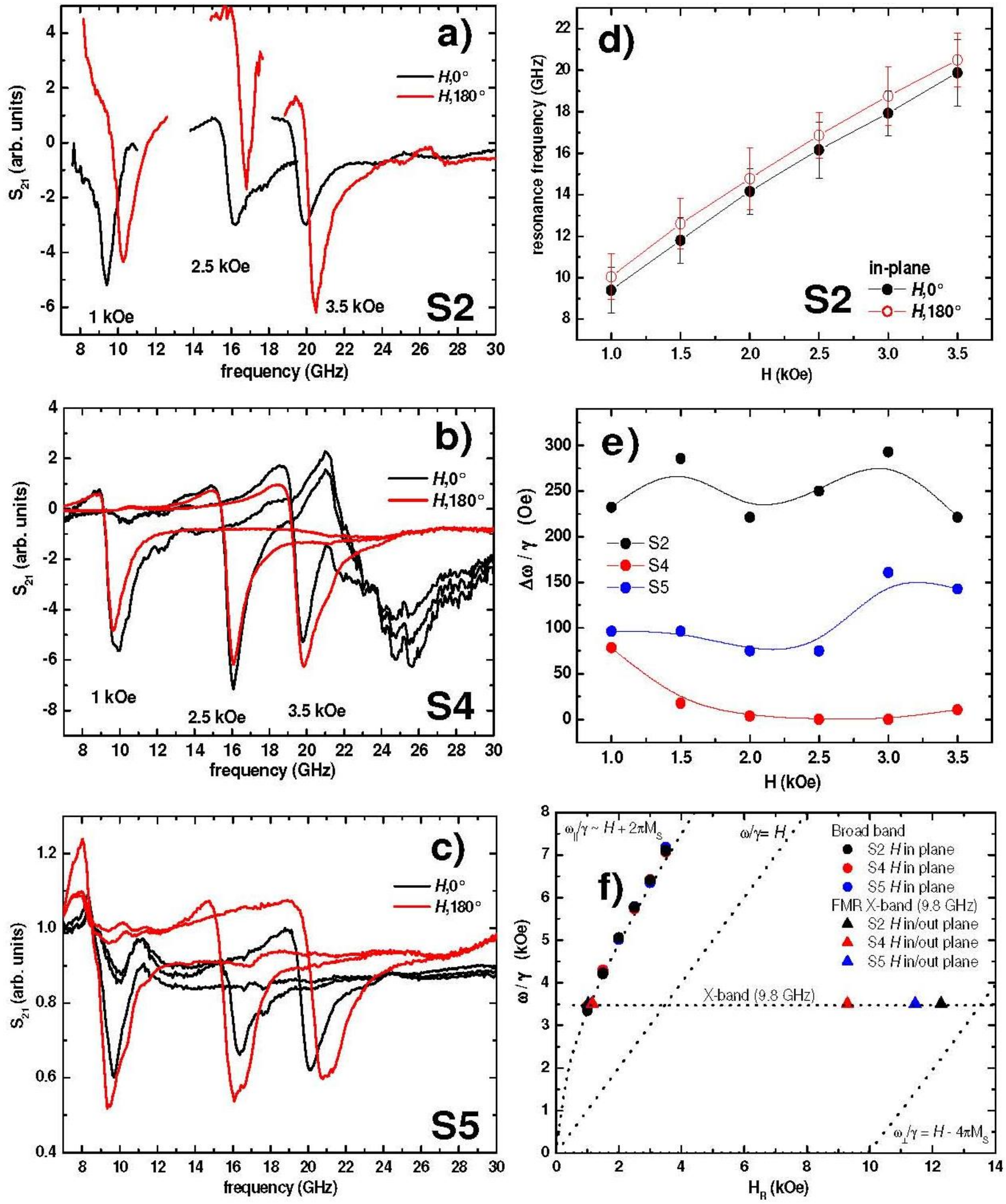

Figure 5.2.5: VNA broadband (1 GHz-30 GHz) measurements at room-T. (Fig. a, b and c) The transmission parameter S21, obtained for each sample at 0° and 180° orientations.(Fig. d) Typical field dependence of the FMR spectra for sample S2, in both in-plane orientations. (Fig. e) Field dependence of the field-gap between both orientations. (Fig.f)) High frequency FMR response of these samples, with the combination of both results: FMR at X-band in-plane and out-plane, and FMR broadband, and the theoretical curves (MS = 800 Oe).

5.3 Conclusions

These results show that these factors, such as, the roughness, crystalline defects and inhomogeneities can be critical factors in the ferromagnetic response at high frequency measurements. In particular, as the thickness of the Py layer is reduced from 80 nm to 20 nm, an important disagreement between the static and dynamic response is observed, with a difference, at least in a factor two, in the effective value of the exchange-bias field. The results presented in this study gives support and reinforce the GMI trends of these samples reported by Garcia *et al*., that can be critical for the implementation of these multilayer systems in future devices.

References

1. Darques, M., et al., *Ferromagnetic nanowire-loaded membranes for microwave electronics.* Journal of Magnetism and Magnetic Materials, 2009. **321**(14): p. 2055-2065.
2. Saib, A., et al., *An unbiased integrated microstrip circulator based on magnetic nanowired substrate.* Ieee Transactions On Microwave Theory And Techniques, 2005. **53**(6): p. 2043-2049.
3. Martin, C.R., *Nanomaterials: A Membrane-Based Synthetic Approach.* Science, 1994. **266**(5193): p. 1961-1966.
4. Martin, C.R., *Membrane-based synthesis of nanomaterials.* Chemistry Of Materials, 1996. **8**(8): p. 1739-1746.
5. Stoner, E.C. and E.P. Wohlfarth, *A mechanism of magnetic hysteresis in heterogeneous alloys.* Philosophical Transactions of the Royal Society of London, 1948. **A240**: p. 599-644.
6. Wernsdorfer, W., et al., *Experimental evidence of the Neel-Brown model of magnetization reversal.* Physical Review Letters, 1997. **78**(9): p. 1791-1794.
7. L. Neel, A., Goephys, 1949. **5**: p. 99.
8. Brown, W.F., Physical Review Letters, 1963. **130**: p. 1677.
9. Knobel, M., et al., *Superparamagnetism and Other Magnetic Features in Granular Materials: A Review on Ideal and Real Systems.* Nanoscience and Nanotechnology, 2008. **8**: p. 2836–2857.
10. Morrish, A.H., *The physical principles of magnetism*. 1980: R. E. Krieger Pub. Co.
11. Smit, J. and H.G. Belgers, *Ferromagnetic resonance absorption in BaFe12O19, a highly anisotropic crystal.* Philips Res. Rep., 1955. **10**: p. 113-30.
12. Wade, T.L. and J.E. Wegrowe, *Template synthesis of nanomaterials.* European Physical Journal-Applied Physics, 2005. **29**(1): p. 3-22.
13. *http://rsbweb.nih.gov/ij/download.html*.
14. Trusca, O.C., et al., *Interaction Effects in Ni Nanowire Arrays.* IEEE Transactions on Magnetics, 2008. **44**(11): p. 2730-2733.
15. Encinas-Oropesa, A., et al., *Dipolar interactions in arrays of nickel nanowires studied by ferromagnetic resonance.* Physical Review B, 2001. **63**(10): p. 104415.
16. Dumitru, I., et al., *Study of magnetic interactions in metallic nanowire networks.* Ieee Transactions On Magnetics, 2005. **41**(10): p. 3361-3363.
17. Hertel, R., *Micromagnetic simulations of magnetostatically coupled nickel nanowires.* Journal of Applied Physics, 2001. **90**(11): p. 5752-5758.
18. Hertel, R. and J. Kirschner, *Magnetization reversal dynamics in nickel nanowires.* Physica B: Condensed Matter, 2004. **343**(1â€"4): p. 206-210.
19. Gao, J.-H., et al., *Magnetization reversal process and magnetic relaxation of self-assembled Fe_{3}Pt nanowire arrays with different diameters: Experiment and micromagnetic simulations.* Physical Review B, 2007. **75**(6): p. 064421.
20. Wang, Z.K., et al., *Spin-Wave Quantization in Ferromagnetic Nickel Nanowires.* Physical Review Letters, 2002. **89**(2): p. 027201.
21. Ebels, U., et al., *Ferromagnetic resonance studies of Ni nanowire arrays.* Physical Review B, 2001. **64**(14).
22. Pike, C.R., *First-order reversal-curve diagrams and reversible magnetization.* Physical Review B, 2003. **68**(10).
23. Spinu, L., et al., *Method for magnetic characterization of nanowire structures.* Ieee Transactions On Magnetics, 2004. **40**(4): p. 2116-2118.
24. Ramos, C.A., et al., *FMR characterization of hexagonal arrays of Ni nanowires.* Journal of Magnetism and Magnetic Materials, 2004. **272â€"276, Part 3**(0): p. 1652-1653.

25. Dumitru, I., et al., *Interaction effects analysis of FMR, spectra on dense nanowire systems.* Ieee Transactions on Magnetics, 2006. **42**(10): p. 3225-3227.
26. Lavin, R., et al., *Magnetic Characterization of Nanowire Arrays Using First Order Reversal Curves.* IEEE Transactions on Magnetics, 2008. **44**(11): p. 2808-2811.
27. Carignan, L.P., et al., *Magnetization Reversal in Arrays of Ni Nanowires With Different Diameters.* Magnetics, IEEE Transactions on, 2009. **45**(10): p. 4070-4073.
28. Rotaru, A., et al., *Interactions and reversal-field memory in complex magnetic nanowire arrays.* Physical Review B, 2011. **84**(13): p. 134431.
29. Ferre, R., et al., *Magnetization processes in nickel and cobalt electrodeposited nanowires.* Physical Review B, 1997. **56**(21): p. 14066-14075.
30. Skomski, R., et al., *Magnetic localization in transition-metal nanowires.* Physical Review B, 2000. **62**(6): p. 3900-3904.
31. Zheng, M., et al., *Magnetic properties of Ni nanowires in self-assembled arrays.* Physical Review B, 2000. **62**(18): p. 12282-12286.
32. Sun, L., et al., *Tuning the properties of magnetic nanowires.* IBM Journal of Research and Development, 2005. **49**(1): p. 79-102.
33. Nogues, J., et al., *Exchange bias in nanostructures.* Physics Reports-Review Section of Physics Letters, 2005. **422**(3): p. 65-117.
34. JimÃ©nez, E., et al., *Emergence of noncollinear anisotropies from interfacial magnetic frustration in exchange-bias systems.* Physical Review B, 2009. **80**(1): p. 014415.
35. Gong, Y., et al., *Determination of magnetic anisotropies, interlayer coupling, and magnetization relaxation in FeCoB/Cr/FeCoB.* Journal of Applied Physics, 2009. **106**(6): p. 063916-7.
36. Sort, J., et al., *Controlling magnetic vortices through exchange bias.* Applied Physics Letters, 2006. **88**(4): p. 042502-3.
37. Sort, J., B. Dieny, and J. NoguÃ©s, *Exchange bias in antiferromagnetic-ferromagnetic-antiferromagnetic structures with out-of-plane magnetization.* Physical Review B, 2005. **72**(10): p. 104412.
38. Jimenez, E., et al., *Role of anisotropy configuration in exchange-biased systems.* Journal of Applied Physics. **109**(7): p. 07D730-3.
39. Gloanec, M., et al., *Dynamical effect in measurement of the exchange-bias field: A consequence of the slow-relaxer mechanism.* Physical Review B, 2009. **80**(22): p. 220404.
40. Dubowik, J., et al., *Temperature dependence of ferromagnetic resonance in permalloy/NiO exchange-biased films.* European Physical Journal B, 2005. **45**(2): p. 283-288.
41. da Silva, R.B., et al., *High frequency magnetoimpedance in Ni[sub 81]Fe[sub 19]/Fe[sub 50]Mn[sub 50] exchange biased multilayer.* Applied Physics Letters, 2009. **94**(4): p. 042501-3.
42. Choi, H.-C., et al., *Antiferromagnetic layer thickness dependence of noncollinear uniaxial and unidirectional anisotropies in NiFe/FeMn/CoFe trilayers.* Physical Review B. **81**(22): p. 224410.
43. Phuoc, N.N., et al., *Permalloyâ€“FeMn exchange-biased multilayers grown on flexible substrates for microwave applications.* Journal of Magnetism and Magnetic Materials, 2009. **321**(17): p. 2685-2690.
44. Abdulahad, F.B., et al., *Exchange Bias Effect on the Relaxation Behavior of the IrMn/NiFe Bilayer System.* Magnetics, IEEE Transactions on. **47**(10): p. 4227-4230.
45. Pike, C.R., A.P. Roberts, and K.L. Verosub, *Characterizing interactions in fine magnetic particle systems using first order reversal curves.* Journal Of Applied Physics, 1999. **85**(9): p. 6660-6667.
46. Stancu, A., et al., *Micromagnetic and Preisach analysis of the First Order Reversal Curves (FORC) diagram.* Journal Of Applied Physics, 2003. **93**(10): p. 6620-6622.

47. Harrison, R.J. and J.M. Feinberg, *FORCinel: An improved algorithm for calculating first-order reversal curve distributions using locally weighted regression smoothing.* Geochemistry Geophysics Geosystems, 2008. **9**: p. 11.
48. Tanasa, R., et al., *First-order reversal curve analysis of spin-transition thermal hysteresis in terms of physical-parameter distributions and their correlations.* Physical Review B, 2005. **71**(1): p. 9.

Vita

The Author was born in India in 1981. He received his Bachelor of Science degree in Physics, Chemistry and Mathematics with Physics and Mathematics as major subjects in the year 2003. Then he went to Banaras Hindu University (Varanasi), India, for higher education and received Master of Science degree in Physics with specialization in Condensed Matter Physics in the year 2005. After that he went to Indian Institute of Technology Delhi and earned Master of Technology degree in Solid State Materials in the year 2008. Then he worked for SanDisk Semiconductor (Shanghai) as RnD Engineer from 2008 to 20010. He joined University of New Orleans in Aug 2010 and has earned Master of Science degree in Applied Physics in 2012.